Materials Advances

ROYAL SOCIETY OF CHEMISTRY

PAPER

View Article Online
View Journal

Cite this: DOI: 10.1039/d6ma00162a

Laser-induced graphene electrode and eco-friendly chitosan–poly(ethylene)glycol–$LiClO_4$ electrolytes for all-solid state flexible supercapacitors

Jadan Resnik Jaleel UC, [a] Somashekara Bhat, *[a] Y. N. Sudhakar [a] and Vipin Cyriac [b]

The growing global demand for flexible, safe, and sustainable energy storage systems has intensified research into advanced materials for next-generation electrochemical devices. In response to this need, the present study focuses on the preparation and characterization of a biopolymer blend electrolyte using chitosan (CS) and poly(ethylene)glycol 8000 (PEG) with lithium perchlorate ($LiClO_4$) incorporated for solid-state supercapacitor applications. The optimal blend composition of 70 wt% CS and 30 wt% PEG (named CP30) was subsequently doped with varying concentrations of $LiClO_4$ (10–50 wt%, named CPLxx, with "xx" representing the weight percentage) to enhance ionic conductivity. Electrochemical impedance spectroscopy (EIS) revealed a maximum room temperature ionic conductivity of 1.27×10^{-4} S cm^{-1} for the CPL40 (70 wt% CS, 30 wt% PEG and 40 wt% $LiClO_4$) composition, attributed to improved segmental mobility and lithium-ion dissociation. Electrochemical stability up to 3.23 V was established *via* linear sweep voltammetry (LSV). Two solid state double layer capacitors were fabricated with this solid electrolyte, employing activated carbon and Laser-induced graphene (LIG) as symmetric electrodes. The activated carbon-based device demonstrated a maximum specific capacitance of 5.32 F g^{-1} at 0.01 A g^{-1}, while the LIG-based device exhibited an areal capacitance of 18.83 mF cm^{-2} at 0.02 mA cm^{-2}. Both systems showed good cycling stability, retaining 84.2% and 89.3% of their initial capacitance after 3000 charge–discharge cycles. Additionally, the LIG-based device maintained 97.8% capacitance retention after 500 mechanical bending cycles, underscoring its flexibility and electrochemical durability. The influence of electrode loading was carefully addressed to enable a fair and meaningful performance evaluation of the two systems. These findings collectively demonstrate the potential of CS–PEG–$LiClO_4$ biopolymer electrolytes integrated with carbon-based electrodes to realize eco-friendly and flexible all-solid-state supercapacitors.

Received 4th February 2026,
Accepted 3rd April 2026

DOI: 10.1039/d6ma00162a

rsc.li/materials-advances

1. Introduction

The growing global demand for sustainable and efficient energy storage systems has gained significant interest in developing environmentally friendly materials for electrochemical devices.[1–3] As renewable energy sources such as solar and wind become increasingly integrated into modern power grids, the intermittent nature of these resources requires better and dependable energy storage solutions. Advanced storage technologies such as supercapacitors and solid-state batteries have become critical to provide uninterrupted power delivery.[4,5]

Among these technologies, electric double-layer capacitors (EDLCs) offer high power density, rapid charge–discharge characteristics, and long cycle life, making them highly attractive for advanced energy storage applications.[6,7] Organic or aqueous liquid electrolytes were used in the traditional EDLC, which suffer from drawbacks including leakage, volatility, flammability, and limited mechanical stability. Solid polymer electrolytes (SPEs) have emerged as a promising alternative due to their safety, flexibility, and potential to overcome the limitations associated with liquid electrolytes.[8,9]

In recent years, biopolymer-based SPEs have gained traction due to their abundance, biodegradability, and compatibility with green chemistry principles.[10–12] Chitosan (CS), a naturally derived polysaccharide obtained from the deacetylated derivative of chitin, which can be sustainably sourced from crustacean shell waste, supports circular economic principles and

[a] Manipal Institute of Technology, Manipal Academy of Higher Education, Manipal, India. E-mail: soma.bhat@manipal.edu
[b] Centre for Interdisciplinary Research, SRM University-AP, Amaravati, India

reduces marine biomass waste streams. In the electrolyte field, CS has garnered particular attention due to its film-forming ability, non-toxicity, and the presence of reactive –OH and $–NH_2$ groups that facilitate ionic interactions.[13] However, pure CS films often suffer from limited mechanical flexibility and low ionic conductivity, which restricts their practical application in energy devices.[14] Polyethylene glycol (PEG) is often incorporated as a plasticizer and co-polymer to address these challenges. PEG enhances the flexibility and amorphous nature of the polymer matrix, promoting ion transport by increasing the segmental mobility of polymer chains.[15] Furthermore, doping the CS–PEG matrix with lithium salts, such as lithium perchlorate ($LiClO_4$), introduces free charge carriers and creates coordination sites for efficient lithium-ion conduction.[16]

Furthermore, in the performance of EDLCs the electrode materials play a crucial role. Traditionally, activated carbon has been the material of choice due to its high surface area and cost-effectiveness. However, it possesses limited mechanical stability due to its powdery morphology, which makes it challenging to integrate it into flexible systems.[17] Recently, laser induced graphene (LIG) has emerged as an electrode material for flexible supercapacitor devices.[18] LIG can be directly converted on polymer substrates by laser irradiation, producing a highly conductive and porous carbon network with strong adhesion, hierarchical porosity, and good mechanical strength.[19] LIG was first reported by Tour *et al.* in 2014, who showed that CO_2 laser irradiation of polyimide yields a porous, conductive, few-layer graphene network with strong adhesion and hierarchical porosity.[18] Initially explored for structural control without detailed electrochemical metrics,[20–22] LIG research shifted toward performance optimization *via* doping,[23] composites,[24] and electrolyte tuning.[25] Over a decade, LIG has evolved from a material novelty to a tunable platform for flexible, high-performance supercapacitors.

Despite its promising qualities, LIG has not yet been thoroughly combined with sustainable, biopolymer-based SPEs. Integration of LIG electrodes with a CS–PEG–$LiClO_4$ solid polymer electrolyte could pave the way for safer, more efficient, and eco-friendly energy storage devices, offering excellent mechanical strength and enhanced ionic transport. This work sets out to fill the gap in research regarding the performance of EDLCs by developing and carefully testing a flexible EDLC system under electrochemical and mechanical stress.

In this work, we develop and systematically investigate CS–PEG-based SPEs modified with $LiClO_4$ to enhance ionic conductivity for potential applications in EDLCs. The polymer blends were first optimised with varying contents of high molecular weight PEG 8000 (PEG), which was selected not merely as a plasticiser but as a structural modifier to fine-tune the hydrogen-bonding network of chitosan, achieving an optimal balance between amorphous content and mechanical stability. Following optimisation, the blends were doped with controlled concentrations of $LiClO_4$ and subjected to comprehensive structural, thermal, and morphological characterisation. The electrochemical stability window (ESW) of the optimised SPE was found to be significantly wider than that typically reported for CS systems,[26,27] enabling safe operation over an extended voltage range. To evaluate device-level performance, EDLCs were fabricated using both activated carbon and Laser-induced graphene (LIG) electrodes. Activated carbon served as a benchmark due to its high surface area and well-established capacitance performance, providing a direct reference for comparison. LIG as a flexible electrode material was incorporated here for the first time with a CS–PEG–$LiClO_4$ electrolyte. Its compatibility with flexible substrates, coupled with excellent mechanical integrity under repeated bending tests, further highlights the potential of this electrolyte system for next-generation flexible solid-state energy storage.

2. Methodology

2.1. Chemicals used

Chitosan (medium molecular weight from crab shells with 75% deacetylation) was procured from Loba Chemie Ltd. Poly(ethylene)-glycol 8000 (PEG) with a molecular weight of 8000 g mol^{-1} was obtained from S.D. Fine Chemicals. Analytical-grade $LiClO_4$ (molecular weight 106.39 g mol^{-1}), utilized for electrolyte enhancement, was sourced from Tokyo Chemical Industry. Activated carbon, used as the electrode material in supercapacitor fabrication, was procured from Kuraray, Japan, and polyvinylidene fluoride (PVDF), used as a binder in electrode preparation, was acquired from Sigma Aldrich. Additionally, *N*-methyl pyrrolidone (NMP), serving as the solvent, and super P conductive carbon black (SPC), serving as a conducting agent, were purchased from Thermo Fisher Scientific. The stainless steel used in preparing the 80 μm thick electrode was purchased from a local vendor. A polyimide (PI) sheet with a thickness of 70 μm, obtained from Dongguan LKT Electronic Tech Co., Ltd, was utilized to prepare LIG. Conductive silver paste (Shilpent) and self-adhesive copper tape (Euro) were used for device fabrication.

2.2. Preparation of CS solution

To prepare the CS stock solution, 1 g of CS was weighed and gradually added to 100 mL of distilled water in a clean glass beaker. The mixture was subjected to continuous magnetic stirring at room temperature to ensure uniform dispersion of the CS particles. Stirring was maintained for 10 minutes, allowing CS to swell and hydrate. After the initial stirring period, 1 mL of glacial acetic acid was slowly added dropwise to the mixture while stirring continuously. The solution was left under constant magnetic stirring for 48 hours at room temperature. After the dissolution, the solution was carefully filtered to remove any undissolved particles, impurities, or insoluble residues.

2.3. Preparation of PEG solution

To prepare the PEG solution, 1 g of PEG was weighed and gradually added to 100 mL of distilled water in a clean glass beaker. The mixture was subjected to continuous magnetic stirring at room temperature to ensure uniform dispersion

Table 1 Composition and nomenclature of CS–PEG blends

Weight of CS (%)	Weight of PEG (%)	Nomenclature
100	0	CP0
90	10	CP10
80	20	CP20
70	30	CP30
60	40	CP40
50	50	CP50

and dissolution of PEG in water. The solution was stirred for 6 hours to allow complete dissolution of PEG. After the dissolution process, the PEG solution was visually inspected to confirm clarity and homogeneity.

2.4. Optimization of the CS and PEG blend ratio

The CS and PEG blend ratio was optimized to achieve the desired electrochemical and flexibility performance. The CS and PEG solutions were mixed in various weight ratios. The ratios are given in Table 1. Each mixture was stirred for 12 hours at room temperature. After stirring, the blended solution was kept inside a vacuum desiccator to degas for 2 hours. Afterwards, it was cast into a Petri dish and kept inside an oven for evaporation at 50 °C. The films were left undisturbed until completely dried. Once thoroughly dried, the CS–PEG blend films were gently peeled from the Petri dish.

The blend optimization was limited to CP50, as higher PEG content beyond this ratio may compromise film integrity, reduce mechanical strength, or hinder electrolyte performance due to excessive plasticization.

2.5. Preparation of $LiClO_4$ based CS PEG SPEs

After optimizing the CS–PEG blend ratio through structural and thermal evaluation, the polymer matrix was further modified with metal salts to enhance ionic conductivity. The CP30 composition was chosen as the host matrix because it offers a favorable balance of high amorphous nature, uniform film formation, and adequate mechanical stability, key factors that support effective salt incorporation and consistent electrochemical behavior.

$LiClO_4$ was added to the CP30 blend in varying weight percentages to investigate the effect of metal salt incorporation. The choice of CP30 is based on XRD and DSC analysis. The different compositions and their corresponding nomenclature are presented in Table 2.

The required amount of $LiClO_4$ was weighed and added to the pre-prepared CP30 solution. The mixture was subjected to continuous magnetic stirring for 12 hours at room temperature to ensure complete dissolution of the salt. Following the stirring process, the solution was transferred to a vacuum desiccator and degassed for 2 hours to eliminate the air bubbles. After degassing, the solution was left undisturbed for 4 hours. The solution was poured into clean Petri dishes and evaporated at 50 °C for 12 hours. Once the solvent had evaporated completely, the dried films were gently peeled off from the Petri dishes and stored. $LiClO_4$ content was limited to 50 wt% (CPL50) because higher salt concentrations can lead to ion-pairing or aggregation, which reduces the number of free charge carriers, ultimately lowering ionic conductivity. Excessive salt content affects the mechanical stability and film-forming ability of the polymer matrix, resulting in brittle or non-uniform films.

Table 2 $LiClO_4$ doping levels and nomenclature of CP30-based blends

Name of the blend	Amount of $LiClO_4$ (wt%)	Nomenclature
CP30	10	CPL10
	20	CPL20
	30	CPL30
	40	CPL40
	50	CPL50

2.6. Characterization of electrolytes

The following sections describe the techniques used to characterize the CS–PEG electrolytes and their $LiClO_4$ doped variants. The characterization of these electrolytes included structural, thermal, surface morphological and electrochemical evaluations. Additionally, the performance of assembled supercapacitor devices was tested to understand the practical applicability of the developed electrolytes.

2.6.1. Fourier transform infrared spectroscopy (FTIR). FTIR was employed to analyze the structural features and molecular interactions within the CS–PEG polymer matrix and its $LiClO_4$-doped variants. The spectra were recorded in the range of 4000 cm^{-1} to 400 cm^{-1} with a resolution of 4 cm^{-1} using a standard attenuated total reflectance (ATR) setup.

2.6.2. X-ray diffraction (XRD). XRD analysis was carried out to investigate the crystalline and amorphous characteristics of the CS–PEG blend films and their lithium-doped counterparts. The measurements were performed using a Rigaku smartlab high-resolution X-ray diffractometer equipped with Cu-Kα radiation with a wavelength (λ) of 1.5406 Å. The diffraction patterns were recorded over a 2θ range of 10° to 80° with a scan rate of 4° min^{-1}.

2.6.3. Thermal analysis. Differential scanning calorimetry (DSC) was conducted to evaluate the thermal transitions and stability of the CS–PEG-based SPEs. The analysis was performed using a PerkinElmer DSC 6000 instrument, controlled *via* Pyris software. Approximately 5–10 mg of each sample was heated from 30 °C to 400 °C at a constant rate of 10 °C min^{-1} under a continuous flow of nitrogen gas.

Thermal stability and decomposition behavior were investigated using thermogravimetric analysis (TGA) on a PerkinElmer STA 6000 instrument controlled by Pyris software. The samples were subjected to heating from room temperature up to 600 °C at a rate of 10 °C min^{-1} under a continuous nitrogen flow to maintain an inert environment.

2.6.4. Surface morphological analysis. The surface and cross-sectional morphologies of the SPE films were analyzed using an EVO MA18 (Carl Zeiss) scanning electron microscope (SEM). Elemental composition analysis was performed using an Oxford X-act energy-dispersive X-ray spectroscopy (EDS) detector. A Bruker Innova SPM atomic force microscope (AFM) was used to investigate the electrolyte films' surface topography and

nanoscale roughness. The measurements were performed in tapping mode with Si (p-doped) cantilevers exhibiting spring constants of 20–80 N m^{-1} and resonant frequencies of 250–300 kHz. All the scans were performed at room temperature. The surface roughness was measured by computing the root mean square (RMS) surface roughness.

2.7. EIS analysis of SPEs

The thickness of the metal-doped solid electrolyte films was measured using a micrometer to ensure the precise dimensional data required for ionic conductivity calculations. EIS measurements of the solid polymer electrolyte films were performed using a Biologic SP150 potentiostat. The electrolyte film with the dimension of 1 cm × 1 cm was placed between two stainless steel (SS) electrodes in a symmetric SS|SPE|SS configuration. The impedance spectra were recorded in the frequency range of 1 MHz to 100 Hz with an AC amplitude of 10 mV at room temperature. The obtained impedance data were plotted as Nyquist plots ($-\mathrm{Im}(Z)$ *versus* $\mathrm{Re}(Z)$). The Nyquist plots were fitted using an equivalent circuit model with the ZFit module in BioLogic EC-Lab software, and the bulk electrolyte resistance (R_b) was obtained from the fitted parameters. The ionic conductivity was measured using eqn (1):

$$\text{Ionic conductivity} = \frac{L}{R \cdot A} \tag{1}$$

where L is the thickness of the solid electrolytes, R is the resistance measured from the Nyquist plot, and A is the area of the electrolyte.

2.8. Linear sweep voltammetry analysis

Linear sweep voltammetry (LSV) measurements were carried out using the polymer electrolyte film sandwiched between two identical stainless steel (SS) electrodes, forming an SS|SPE|SS configuration. The potential was linearly swept from 0 V to 5 V at a scan rate of 10 mV s^{-1}.

2.9. Transference number measurement study

Transference number measurements (TNM) were carried out on the highest conducting SPE films at room temperature using a biologic SP150 potentiostat. SS electrodes were arranged in a symmetric SS|SPE|SS configuration. A constant potential of 100 mV was applied, and the current was monitored over time to provide insights into the electrochemical behavior and ion transport characteristics of the SPE films.

2.10. Fabrication and performance analysis of EDLC devices

The preparation of the supercapacitor devices involved the fabrication of electrodes using activated carbon. Activated carbon, SPC and PVDF were mixed in the weight ratio of 8 : 1 : 1. NMP was added to the mixture to form a homogeneous paste. This paste was uniformly coated onto a 1 cm × 1 cm stainless-steel electrode and later dried in an oven at 50 °C. Two prepared electrodes were assembled into a symmetric device configuration, with a CPL40 layer placed between them. The devices were named SC-1.

LIG was prepared by adjusting laser parameters such as power (40 W) and speed (180 mm s^{-1}) over a 2 cm × 2 cm area, following the method reported previously.[25] As in the case of the activated carbon device, two LIG electrodes were assembled into a symmetric configuration with a CPL40 electrolyte between them. The device was named SC-2. The complete procedure of synthesis and fabrication is given in Fig. 1.

The performance of SC-1 and SC-2 was evaluated using CV, GCD, and EIS techniques. All electrochemical characterization was performed using a SP Biologic 150 potentiostat. CV was performed at various scan rates in the potential window of 0 V to 1.3 V. The GCD characteristics of SC-1 were determined at current densities of 0.01–0.1 A g^{-1} and those of SC-2 at 0.02–0.25 mA cm^{-2}. EIS was performed from 1 MHz to 100 mHz using an AC voltage of 10 mV.

Eqn (2) and (3) were used for calculating the specific capacitance of SC-1, and (3) and (4) were used for calculating the areal capacitance of SC-2.

From CV,

$$\text{Specific capacitance } (C_A) = \frac{\int i\mathrm{d}v}{vm\Delta V} \tag{2}$$

where $\int i\mathrm{d}v$ is the area of the CV curve, v is the scan rate used in the study, m is the mass load on the electrode and ΔV is the potential window used.

From GCD,

$$\text{Specific capacitance } (C_A) = \frac{i\Delta t}{S\Delta V} \tag{3}$$

where i is the current (mA) and Δt is the discharge time excluding the IR drop.

From CV,

$$\text{Areal capacitance } (C_A) = \frac{\int i\mathrm{d}v}{vS\Delta V} \tag{4}$$

where $\int i\mathrm{d}v$ is the area of the CV curve, v is the scan rate used in the study, S is the active area of the electrode and ΔV is the potential window used.

From GCD,

$$\text{Areal capacitance } (C_A) = \frac{i\Delta t}{S\Delta V} \tag{5}$$

where i is the current (mA) and Δt is the discharge time excluding the IR drop.

Additionally, the energy and power densities were calculated using eqn (6) and (7):[31]

$$\text{Energy density } (E) = \frac{(\Delta V^2)C_A}{2 \times 3600} \tag{6}$$

$$\text{Power density } (P) = \frac{3600E}{\Delta t} \tag{7}$$

2.11. Flexibility and cyclic stability test

The mechanical flexibility of the SC-2 device was evaluated through repeated bending tests. The device was bent from its nearly flat configuration (approximately 178°) to a curved

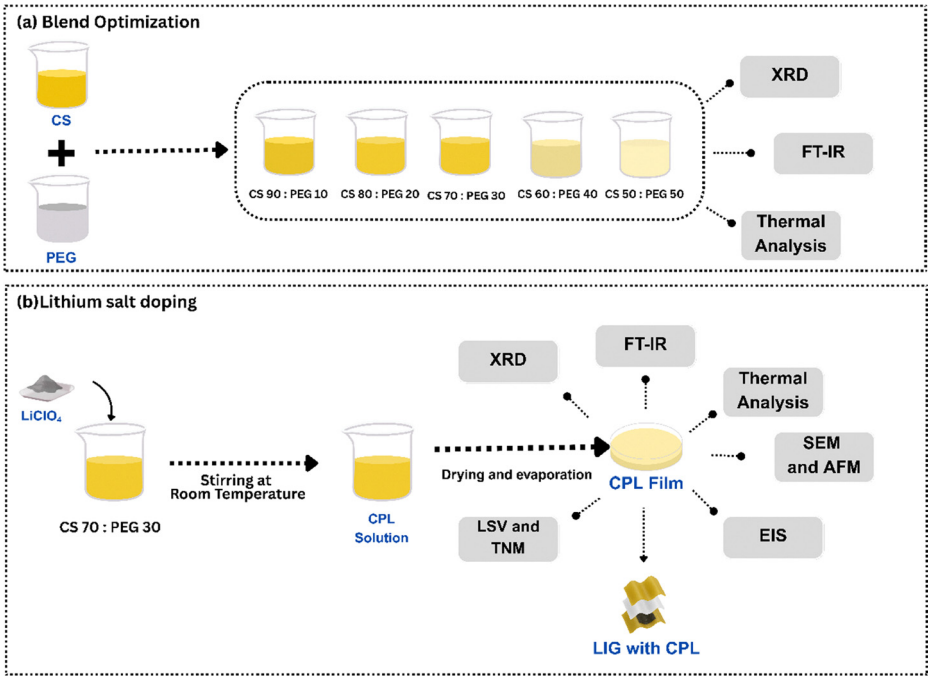

Fig. 1 Schematic representation of the preparation, optimization, and characterization of (a) CS-PEG blend and (b) $LiClO_4$-doped CS-PEG (CPL) film with LIG integration.

configuration with a bending angle of approximately 75° and then returned to its original position. This bending and release process was considered as one cycle. The procedure was repeated for up to 500 cycles to evaluate the mechanical durability of the device. Electrochemical performance was evaluated by recording CV measurement after every 100 bending cycles at a scan rate of 10 mV s^{-1}, GCD was recorded before bending and after 500 bending cycles, and the capacitance retention was calculated to evaluate the effect of repeated mechanical deformation on device performance.[28,29]

Also, the cyclic stability of the SC-1 device was assessed by GCD cycling at a constant current density of 0.05 A g^{-1} for 3000 cycles. The SC-2 device was assessed at a current density of 0.125 mA cm^{-2}. Capacitance retention and coulombic efficiency were calculated throughout the cycling test to evaluate the long-term electrochemical stability of the electrodes in combination with the CS–PEG–$LiClO_4$ solid biopolymer electrolyte.

3. Results and discussion

The CS–PEG blend films were prepared according to the compositions listed in Table 1. The following characterization techniques were performed to study their properties and determine the optimal ratio.

3.1. FTIR

FTIR spectroscopy was used to investigate the molecular interactions and structural organisation within the CS–PEG and CS–PEG–$LiClO_4$ solid polymer electrolytes. In the CS–PEG blends, CS provides primary amine and hydroxyl groups, while PEG contributes ether linkages and terminal hydroxyl functionalities. These functional groups readily form hydrogen bonds, which are central to miscibility, structural cohesion, and segmental mobility. In the $LiClO_4$-doped blends, Li^+ ions coordinate with electron-rich ether oxygens in PEG and amino/hydroxyl groups in CS, while perchlorate anions (ClO_4^-) introduce distinct low-wavenumber features. Such polymer–ion interactions restructure the original hydrogen-bonding network, alter chain packing, and promote ion transport.

Fig. 2 presents the FTIR spectra of CS–PEG blends (CP0–CP50) and $LiClO_4$-incorporated CS–PEG blends (CPL0–CPL50). These spectra show the major vibrational bands corresponding to functional groups present in the polymer matrices and their evolution with composition. The key peak assignments, along with concise inferences regarding the interactions they represent, are summarised in Table 3.

These cumulative FTIR observations demonstrate that PEG incorporation and lithium salt doping significantly alter the hydrogen bonding network, enhance polymer flexibility, and promote ion coordination. These interactions are more than just structural; they play a crucial role in the ionic conduction mechanism. The observed spectral changes thus not only confirm miscibility but also highlight the functional contribution of polymer–ion and polymer–polymer interactions to electrolyte performance. The structural rearrangements evidenced by FTIR analysis directly correlate with improvements in ionic conductivity and electrochemical performance, validating the effectiveness of CS–PEG–$LiClO_4$ systems as promising SPEs for energy storage applications.

The schematic in Fig. 3 illustrates the supramolecular organization of the CS–PEG–$LiClO_4$ hybrid electrolyte, emphasizing the

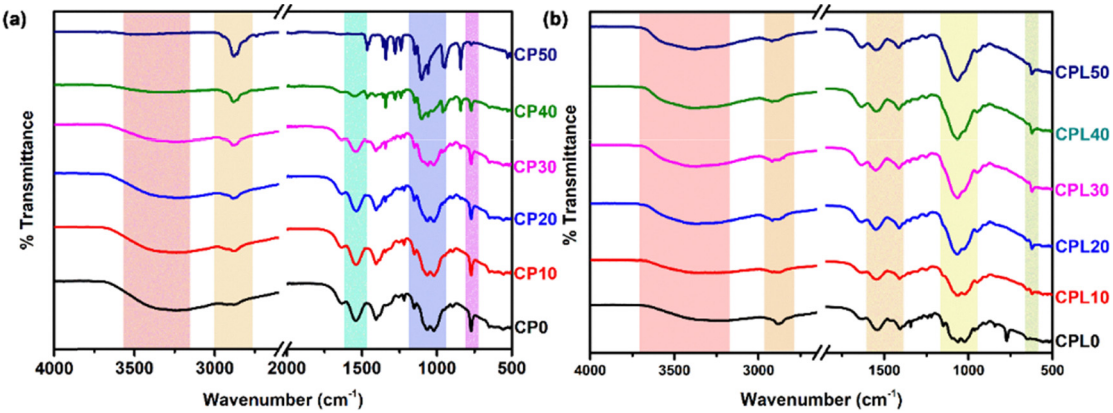

Fig. 2 FTIR spectra of (a) CS–PEG blends (CP0–CP50), showing characteristic absorption bands corresponding to functional groups and (b) $LiClO_4$ incorporated blends (CPL0–CPL50).

Table 3 FT-IR wavenumbers for CP and CPL films with functional group assignments and inferences

Functional group	CP0	CP10	CP20	CP30	CP40	CP50	CPL0	CPL10	CPL20	CPL30	CPL40	CPL50	Inference
	Wavenumber (cm^{-1})												
O–H/N–H stretching	3249	3241	3240	3263	3280	3274	3263	3276	3279	3256	3274	3276	Shift to higher wavenumber with PEG, Li^+ coordination reduces H-bonding strength
C–H symmetric stretching	2921	—	—	—	—	—	—	2917	2918	2918	2919	2920	Disappears in CP blends after CP0; reappears with $LiClO_4$, indicating an altered chain environment
C–H asymmetric stretching	2881	2877	2884	2884	2883	2881	2884	2882	2882	2883	2884	2882	Minor changes; backbone is largely intact, local packing affected by PEG/Li^+
C═O stretching (amide I)	1632	1632	1632	1632	1632	1639	1632	1632	1632	1632	1632	1632	Backbone stable: slight upshift in CP50; unaffected by Li^+
N–H bending (primary amine)	1542	1541	1537	1542	1550	1535	1542	1546	1548	1552	1547	1548	Small shifts with PEG; upward shift in CPL blends indicates stronger amine–Li^+ interaction
–CH_2 bending	—	—	—	1468	1467	1466	1468	—	—	—	—	—	Appears from CP30; disappears after $LiClO_4$ addition due to CH_2 environment disruption
–CH_3 bending	1407	1406	1406	1407	1411	1413	1407	1409	1411	1413	1414	1414	Minor shifts; slight conformational changes with PEG/Li^+
C–N stretching (amide III)	—	1343	1343	1343	1342	1341	1343	1348	1349	1349	1349	1350	Emerges from CP10; upward shift in CPL blends due to Li^+–amide coordination
Hydroxyl bending (CS)	1256	1253	1243	1242	1241	1240	—	—	—	—	—	—	PEG–hydroxyl interactions in CP blends; suppressed in CPL blends due to Li^+ binding
Asymmetric C–O–C stretching	1152	1151	1150	1149	1148	1147	1242	1252	1252	1252	1252	1252	Ether oxygens interact with PEG in CP blends; coordinate with Li^+ in CPL blends
C–O stretching	1065	1065	1063	1061	1060	1060	1061	1062	1066	1065	1061	1063	Slight shift; hydrogen bonding and backbone affected by PEG/Li^+
C–O stretching	1020	1021	1021	1022	—	—	1022	1022	—	—	—	—	Disappears in CP40–CP50; absent at high $LiClO_4$
C–O–C bending	—	—	—	—	960	947	—	—	—	—	—	—	Appears at high PEG content; not observed in CPL blends
C–H ring bending (monosaccharide)	896	897	896	899	—	—	899	895	—	—	—	—	Present at low PEG content; lost at high PEG and in CPL blends
CH_2 rocking (out-of-plane)	—	—	841	842	841	841	842	—	—	—	—	—	Appears from CP20; lost after $LiClO_4$ addition
C–C skeletal vibration	772	772	772	772	772	771	772	—	—	—	—	—	Backbone preserved in CP blends; diminished in CPL blends
$LiClO_4$ skeletal vibration	—	—	—	—	—	—	—	620	621	621	621	620	ClO_4^- band appears only in $LiClO_4$-containing blends

synergistic non-covalent interactions leading to its structural and electrochemical properties. The flexible polyether backbone of PEG coordinates Li^+ (blue dashed lines) *via* ether oxygens, promoting ion dissociation and migration, while the chitosan backbone offers additional Li^+ coordination through hydroxyl and amino groups, enhancing transport and providing mechanical stability. ClO_4^- anions (red) form hydrogen bonds (red dashed lines) with PEG hydroxyls and protonated CS amines, stabilizing the network without stopping the movement of Li^+. This dual-network architecture integrates the segmental mobility of PEG with CS rigidity, yielding a robust, ion-conductive matrix with improved Li^+ transference, reduced crystallinity-related barriers, and enhanced electrochemical stability for flexible solid-state energy devices.

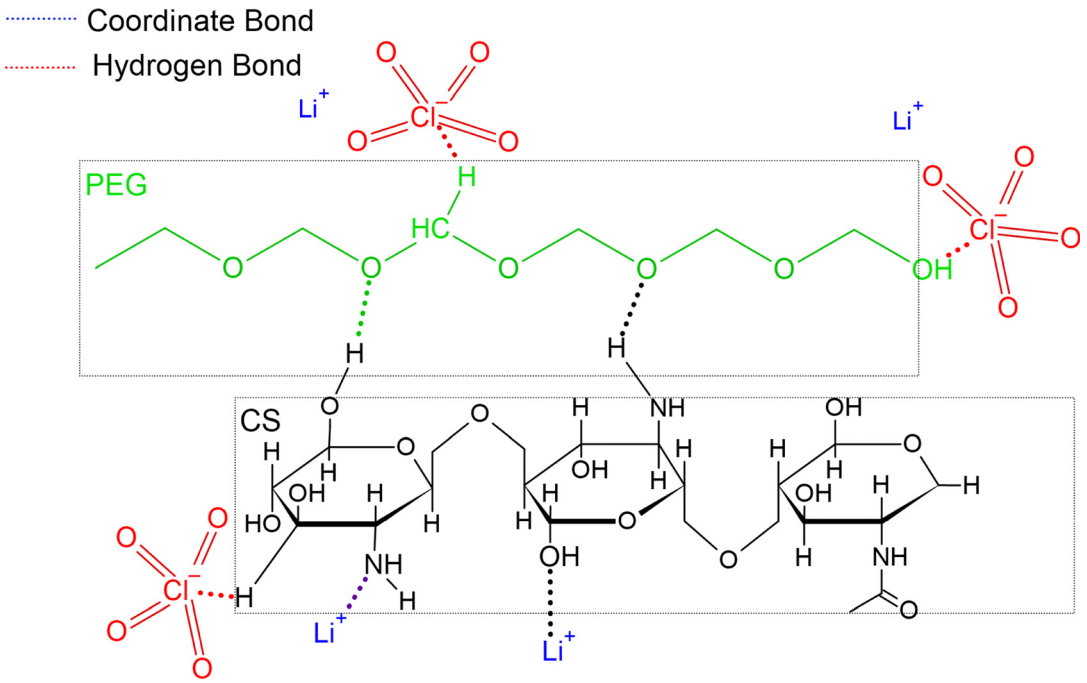

Fig. 3 Structure of CS–PEG–$LiClO_4$ showing Li^+ coordination and ClO_4^- hydrogen bonding within the hybrid network.

3.2. XRD

XRD analysis was carried out to evaluate the crystalline and structural organization of the CS–PEG polymer blend system across varying compositions. The evolution of diffraction patterns with PEG incorporation provides insights into phase transitions, miscibility, and the extent of molecular ordering within the blends.

3.2.1. XRD analysis of the CS–PEG blend. The XRD patterns of the CS–PEG blend films (CP0 to CP50) are depicted in Fig. 4. The structural evolution of the polymer matrix with increasing PEG content was examined by tracking the presence, shift, and suppression of characteristic diffraction peaks associated with CS and PEG.

Pure CS (CP0) exhibited broad diffraction features, notably a broad halo centered around $2\theta = 20^\circ$, which is a hallmark of its predominantly amorphous nature.[26] Additionally, weak crystalline features corresponding to CS's semi-crystalline domains were observed at $2\theta \approx 11^\circ$, 16.5°, 18°, and 21.5°, in agreement with literature reports.[27,30] These reflections originate from inter- and intra-chain hydrogen bonding within the CS matrix and are indicative of ordered packing between CS chains. PEG is known to exhibit sharp crystalline peaks, with the most prominent reflections appearing at $2\theta = 19.08^\circ$ and 23.1°. These peaks become increasingly evident in the blends as PEG content increases. Beginning with CP10, a faint shoulder around 19° and a small peak near 23° appear, confirming the partial incorporation and crystallization of PEG within the CS matrix.

In CP10 and CP20, both CS and PEG crystalline features coexist, though CS peaks begin to diminish in intensity, indicating partial disruption of CS's ordered regions by PEG. In the CP30 sample, a significant reduction in peak intensity is observed across the entire 2θ range, especially in the region corresponding to PEG's crystalline peaks. This decrease in

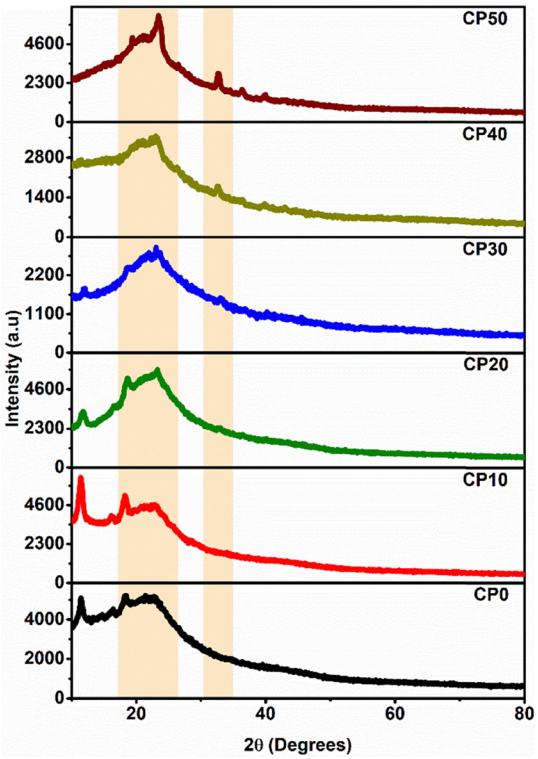

Fig. 4 XRD spectra of samples with variable compositions CP0, CP10, CP20, CP30, CP40, and CP50. Shaded areas indicate regions where peak position and intensity vary, reflecting changes in crystallinity.

diffraction intensity suggests a highly disordered, amorphous structure. The suppressed crystallinity at this composition indicates enhanced miscibility and molecular-level blending, resulting in minimal phase separation and the lowest degree of crystalline ordering among the blends.[31] Thus, CP30 represents a compositionally optimized blend with maximum amorphous character, likely due to the saturation of interaction sites and disruption of both CS and PEG crystallites. In CP40 and CP50, the dominance of PEG crystallinity is evident, with sharp peaks at 19° and 23°, while CS peaks are entirely absent. This structural transition is attributed to the plasticizing effect and hydrogen bonding interactions between PEG and CS, which disrupt CS's crystalline domains and promote PEG crystallite formation.[32]

3.2.1.1. XRD analysis of CS–PEG–$LiClO_4$. To investigate the structural influence of $LiClO_4$ doping on the CS–PEG matrix, XRD analysis was performed for CPL0 to CPL50, as shown in Fig. 5. The incorporation of $LiClO_4$ induces notable changes in crystalline, reflecting the polymer–salt interactions and ionic coordination behavior within the blend system.

The CPL0 sample (without $LiClO_4$) exhibits a broad amorphous halo centred around $2\theta \approx 20°$, characteristic of a disordered polymer blend with partial short-range ordering from PEG segments. No sharp peaks corresponding to salt or polymer crystallinity are visible in this composition.

Upon the introduction of $LiClO_4$, the XRD patterns evolve distinctly. In CPL10 and CPL20, new sharp peaks appear at approximately 21.2°, 23.6°, and 26.6°. These peaks closely match the known diffraction angles of pure crystalline $LiClO_4$ reported at 21.21°, 23.74°, and 26.56°, confirming the partial retention of $LiClO_4$ crystallinity in the matrix at these loading levels.[33,34] The presence of these peaks indicates that some $LiClO_4$ remains in an uncoordinated or weakly interacting crystalline form. In CPL30, the intensities of these peaks begin to decrease, and the background halo becomes more prominent. This suggests the onset of disruption in salt crystallinity, potentially due to increasing interactions between Li^+ ions and polar sites on the CS and PEG chains.

Notably, in CPL40 and CPL50, the sharp peaks at 21.2°, 23.6°, and 26.6° are either significantly weakened or completely absent. The resulting XRD profiles return to a broad, amorphous-like pattern, indicating enhanced salt dispersion and molecular-level complexation. The disappearance of salt reflections implies that Li^+ ions are now largely coordinated within the polymer matrix, forming a polymer–salt amorphous network and suppressing long-range order.

This progressive amorphization with increasing $LiClO_4$ content – particularly evident in CPL40 – suggests that the salt is no longer phase-separated but molecularly integrated. Such a structure is considered beneficial for improving ionic transport, as explored further in the next section on ionic conductivity.

3.2.2. Thermal analysis. Thermal analysis, including DSC and TGA, was performed to examine the thermal transitions and stability of the synthesized polymer electrolytes. DSC was used to identify glass transition behavior, while TGA assessed thermal degradation profiles.

3.2.2.1. DSC analysis. The DSC analysis of CS-based blends was carried out to investigate the influence of PEG and lithium perchlorate on the thermal behavior of the materials. Fig. 6(a) (CP series) and Fig. 6(b) (CPL series) display the DSC thermograms of these systems, with the corresponding glass transition temperatures (T_g) determined using the tangent method summarized in Table S1. The procedure for calculating T_g by the tangent method is illustrated in Fig. S1 for the CP series and in Fig. S2 for the CPL series.

For the CP series the pure CS sample (CP0) displayed a T_g of 55.3 °C, characteristic of a moderately rigid polymeric matrix resulting from strong intermolecular hydrogen bonding between CS chains. Upon the introduction of PEG, T_g initially increased to 52.1 °C for CP10, suggesting that moderate PEG incorporation may promote additional hydrogen bonding interactions or partial network stabilization, thereby reducing chain mobility. However, with further PEG addition, the T_g values showed a variable pattern, with CP20 at 55.2 °C, CP30 at 50.8 °C, and CP40 at 51.8 °C. This behavior suggests a complex balance between the plasticization effect of PEG, which disrupts CS–CS interactions, and the formation of PEG–CS hydrogen bonds. At higher PEG contents, the plasticizing action dominates, enhancing chain flexibility and promoting a more amorphous and less crystalline structure, beneficial for improved segmental mobility.

In the CPL series, the pure CS–PEG blend (CPL0) showed a T_g of 50.8 °C. Upon addition of lithium perchlorate salt, a variable T_g pattern was observed, reflecting changes in ionic coordination within the polymer matrix. CPL10 and CPL20 exhibited T_g values of 51.7 °C and 51.1 °C, respectively, indicating a reduction in chain rigidity due to lithium perchlorate disrupting hydrogen bonding interactions and enhancing polymer segmental mobility. However, CPL30 and CPL40 exhibited elevated T_g values of 50.8 °C and 48.3 °C, respectively.

The variations observed in T_g after $LiClO_4$ incorporation can be due to the coordination interactions between Li^+ ions and

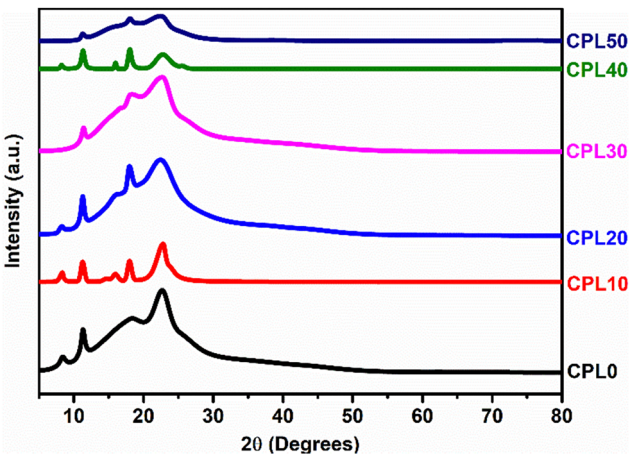

Fig. 5 XRD patterns of CS–PEG-based SPEs (CPL0–CPL50) with varying $LiClO_4$ content.

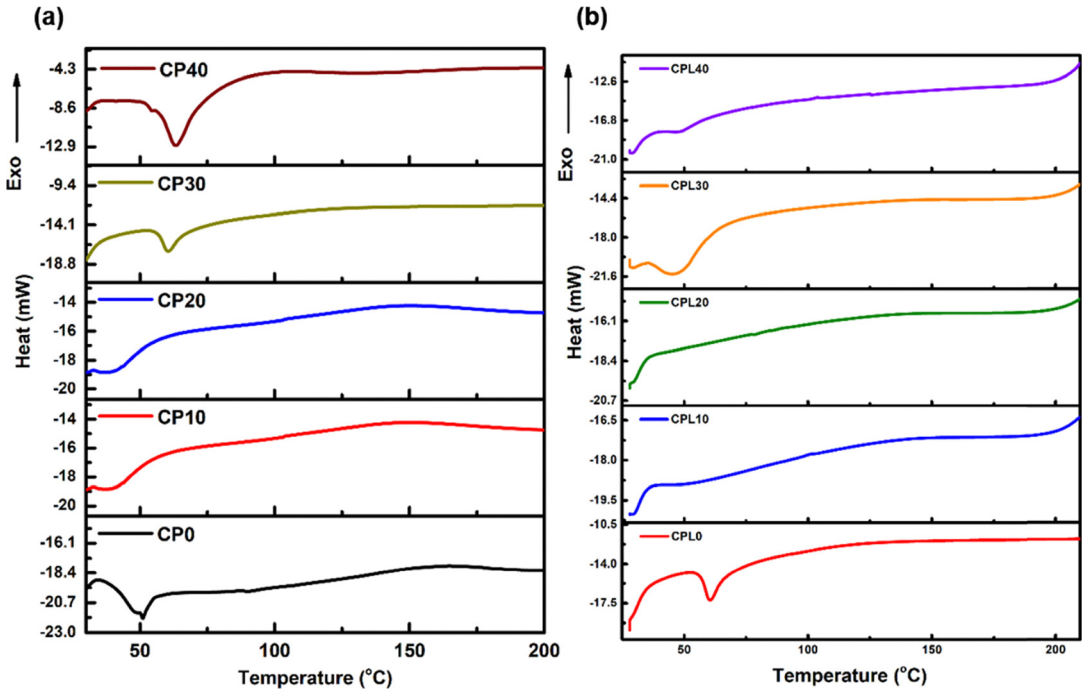

Fig. 6 DSC thermograms of (a) CS–PEG blends and (b) CS–PEG–$LiClO_4$.

the polar functional groups present in the CS–PEG matrix. Such polymer–salt interactions can influence polymer chain mobility by introducing localized ionic interactions within the polymer network. Direct structural evidence for these interactions is provided by the FTIR and XRD results. FTIR shows shifts in the characteristic polymer bands after $LiClO_4$ incorporation, confirming coordination of Li^+ ions with the polar functional groups of the CS–PEG matrix, while XRD shows progressive suppression of the crystalline $LiClO_4$ reflections and enhanced amorphization with increasing salt content. Together, these results support localized polymer–ion interactions that influence chain mobility and thereby contribute to the observed T_g variation.[35]

Overall, these results confirm that PEG acts as an effective plasticizer for CS, reducing crystallinity and increasing flexibility,[36] while lithium perchlorate introduces competing ionic interactions that can either reinforce or weaken the polymer network depending on its concentration.[37] Such glass transition behavior is highly valuable for optimizing these biopolymer systems in electrochemical applications.[38]

In selecting the host polymer matrix for salt incorporation, CP30 was chosen based on a combined assessment of thermal and structural characteristics rather than T_g alone. Although CP40 exhibits a comparable T_g, XRD analysis showed that CP30 possesses the highest amorphous content with minimal PEG crystallinity, along with better film homogeneity and mechanical integrity. These features are essential for uniform salt dispersion and stable ion transport, making CP30 a more suitable host matrix for subsequent lithium salt doping.

3.2.2.2. TGA analysis. The thermal stability and degradation behavior of the prepared SPE films were evaluated by TGA (Fig. 7). All samples, irrespective of lithium perchlorate content, exhibited a multi-step decomposition pattern across the measured temperature range.

The initial weight loss, observed between 40 °C and 120 °C, ranged from 10% to 16%, which is primarily attributed to the evaporation of the residual acetic acid solvent and the desorption of moisture bound to the polymer matrix.[39] In particular, the water molecules are likely associated with polar functional groups such as hydroxyl (–OH) and amine ($–NH_2$) present in CS and PEG.[40,41] These groups form weak hydrogen bonds that break easily at low temperatures, resulting in early-stage mass loss.[42]

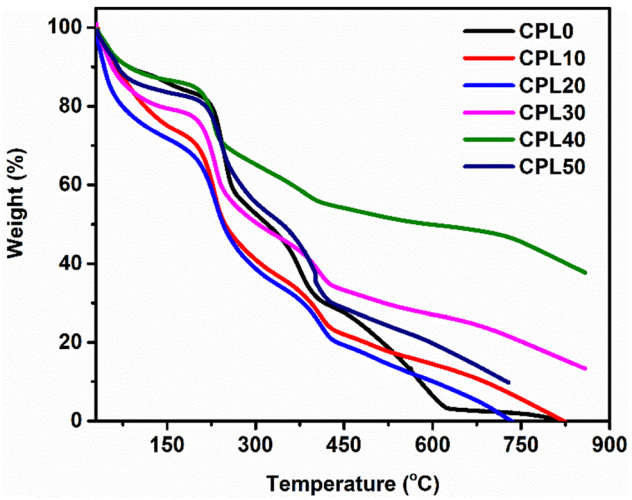

Fig. 7 TGA curves of the CPL series.

The second stage of decomposition occurred within the temperature range of 120 °C to 310 °C, characterized by a more substantial mass reduction, making it the major decomposition. This stage corresponds to thermal cleavage of the polymer backbone, involving chain scission reactions and the disruption of ionic interactions between the polymer and the lithium perchlorate salt. The presence of Li^+ ions may have initially contributed to polymer stabilization through ionic crosslinking; however, at elevated temperatures, the weakening of these interactions facilitates degradation.[43]

A third major degradation stage was identified between 450 °C and 600 °C, corresponding to the thermal decomposition of residual organic matter and char. In this region, a further 20% mass loss was observed, signaling the near-complete breakdown of the polymeric components. Notably, the decomposition temperature (T_d) showed a downward trend with increasing lithium salt concentration.[30] This thermal destabilization can be attributed to the interaction between the polymer matrix and the dopant salt. As lithium perchlorate content increases, the salt may interfere with the structural integrity of the polymer, weakening the network and reducing the thermal resistance.

Further, the number of decomposition stages varied with salt concentration. Samples with moderate doping levels, such as CPL20 and CPL30, displayed a three-step degradation profile, suggesting a more sequential breakdown mechanism. In contrast, highly doped samples like CPL40 and CPL50 exhibited only two distinct decomposition steps, indicating a more rapid and overlapping thermal decomposition process. This change is likely due to the accelerated degradation of the perchlorate anion, which releases reactive by-products such as chlorine and oxygen, promoting aggressive chain breakdown and reducing the resolution of thermal events.

Despite the observed variations, all polymer electrolyte samples retained decomposition onset temperatures above 150 °C, confirming their thermal adequacy for potential use in energy storage devices that demand moderate thermal stability during operation.

3.2.3. Ionic conductivity analysis of SPEs. The electrochemical performance of the CPL polymer electrolytes was evaluated using EIS (Fig. 8). In the Nyquist plots, the experimental data (black circles) were fitted using equivalent circuit models (red line). For CPL10 and CPL20, the impedance spectra exhibit a small semicircle followed by a linear tail. Therefore, the data were fitted using the circuit shown in Fig. 8(f) consisting of $Q1 + (Q2/R1)$. In contrast, the spectra for CPL30–CPL50 display predominantly linear behavior without a distinct semicircle and were fitted using the circuit $R1 + Q1$ shown in Fig. 8(g) (the plus sign (+) between the circuit symbols indicates series arrangement, whereas the slash sign (/) indicates parallel arrangement).

The extracted equivalent circuit fitting parameters, including bulk resistance ($R1$ or R_b), constant phase element parameters ($Q1$, $Q2$) and the normalized χ^2 values, are summarized in Tables S2 and S3. The CPE elements represent the non-ideal capacitive behavior arising from interfacial heterogeneity and distributed relaxation processes in the polymer electrolyte. The low normalized χ^2 values indicate a good agreement between the experimental impedance data and the fitted equivalent circuit model.

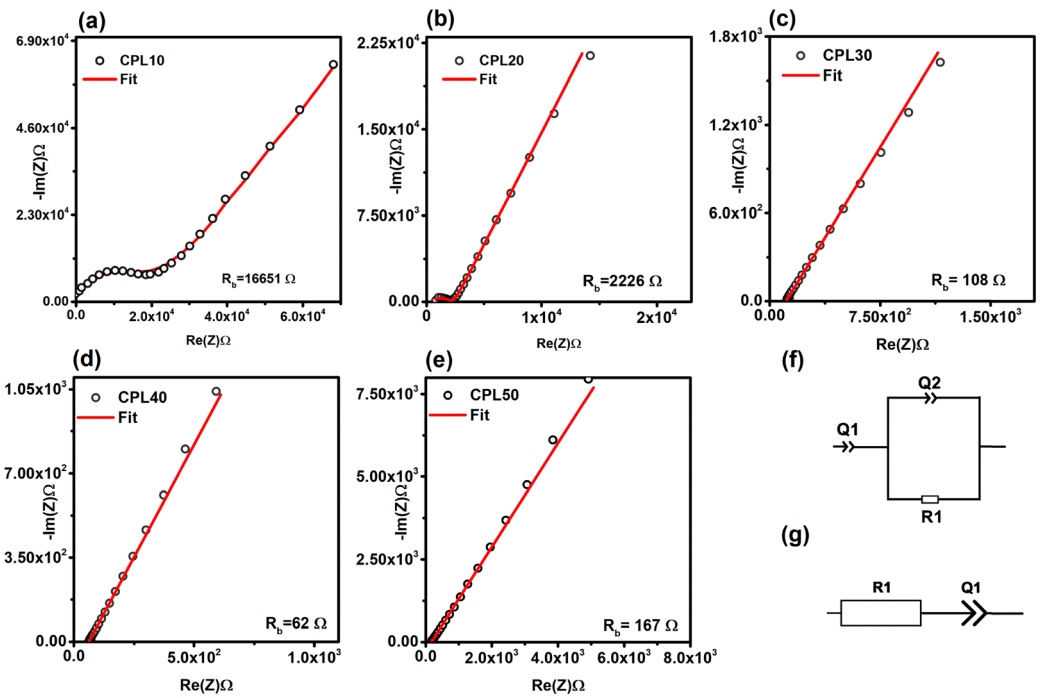

Fig. 8 Nyquist plots and fitting curves for sample (a) CPL10, (b) CPL20, (c) CPL30, (d) CPL40, and (e) CPL50, demonstrating the variation in bulk resistance (R_b) with salt content, and (f) equivalent electrical circuit model used for fitting the impedance data.

Table 4 Calculated ionic conductivity values of SPEs

SPE sample	Thickness (μm)	R_b value (kΩ)	IC (μS cm^{-1})
CPL10	57.75	16.651	0.347
CPL20	52.75	2.226	2.37
CPL30	58.75	0.108	54.40
CPL40	78.75	0.062	127.00
CPL50	90.75	0.167	54.3

The extracted R_b values demonstrate a significant reduction from 16.651 kΩ in CPL10 to 62 Ω in CPL40, followed by a slight increase to 0.167 kΩ in CPL50, indicating the dependence of ionic transport on polymer composition. The ionic conductivity values (calculated using eqn (1)), bulk resistance and thickness of the samples are given in Table 4.

CPL10 exhibits the lowest conductivity of 0.347 μS cm^{-1}, progressively increasing to 127 μS cm^{-1} in CPL40, marking the highest ionic conductivity among the samples. The improvement in conductivity is attributed to increased polymer chain flexibility and enhanced lithium-ion mobility due to PEG incorporation.[44]

The increase in ionic conductivity from 0.347 μS cm^{-1} (CPL10) to 127 μS cm^{-1} (CPL40) can be correlated with the progressive strengthening of polymer–salt interactions and the increase in amorphous character. FTIR results show measurable shifts in the O–H/N–H, N–H, and C–N bands upon $LiClO_4$ incorporation, with the N–H bending band shifting from 1542 cm^{-1} in CPL0 to 1546–1552 cm^{-1} in the salt-containing films and the C–N band shifting from 1343 cm^{-1} to 1348–1350 cm^{-1}, indicating Li^+ coordination with the CS–PEG matrix. In parallel, the crystalline $LiClO_4$ reflections observed at 21.2°, 23.6°, and 26.6° become progressively weakened with increasing salt content and are strongly suppressed in CPL40, indicating improved salt dispersion and enhanced amorphization. However, despite further salt addition, the conductivity decreases to 54.3 μS cm^{-1} for CPL50. Since no substantial additional FTIR shift is observed beyond CPL40, this suggests saturation of the available coordination sites, while the reduced conductivity is consistent with excess-salt-induced ion association or aggregation, which lowers the concentration of free mobile ions.

3.2.4. Surface morphological analysis. The surface and cross-sectional morphologies of the polymer electrolytes were examined using SEM, as shown in Fig. 9. The images of CP30 (Fig. 9(a) and (b)) exhibit a relatively smooth surface with minimal porosity, indicating a dense polymer matrix with limited phase separation. Small, dispersed pores suggest the initial structural modifications due to PEG incorporation, which influences flexibility but does not significantly enhance transport pathways. In contrast, the surface morphology of CPL40 (Fig. 9(c) and (d)) reveals a significant increase in porosity, with uniformly distributed pores across the polymer matrix. The enhanced porosity suggests improved phase separation and the formation of interconnected channels, which are essential for facilitating lithium-ion mobility within the electrolyte.

Despite the increased porosity observed in CPL40, AFM analysis (Fig. 10) indicates that CPL40 exhibits lower surface roughness (24–32 nm) compared to CP30 (39–45 nm). This suggests that although CPL40 has a more interconnected porous network, its surface texture is relatively smooth at the nanoscale due to a more uniform polymer phase distribution.[45]

The combination of SEM and AFM results confirms that porosity does not necessarily correlate with higher roughness, as the polymer reorganization in CPL40 leads to a more homogeneous structure with reduced nanoscale roughness. The cross-sectional images of CPL40 (Fig. 9(e) and (f)) further confirm the highly porous and interconnected bulk structure of the electrolyte. The relatively low surface roughness observed from the AFM analysis indicates a more homogeneous distribution of the polymer–salt complex across the electrolyte surface.[46] Such structural uniformity reduces localized barriers for ion transport and promotes continuous ion-conduction pathways within the polymer matrix,[47] thereby contributing to the higher ionic conductivity observed for the CPL40 composition. The presence of well-defined voids and interconnected pores indicates a reduction in segmental constraints, which is expected to enhance ion conduction by providing continuous transport pathways within the electrolyte matrix, consistent with the ionic conductivity trends obtained from EIS analysis.[48]

3.2.5. LSV. Fig. 11(a) presents the LSV curve of the CPL40 polymer electrolyte, evaluating its electrochemical stability window. The current remains negligible at lower potentials and rises sharply at 3.23 V, indicating the start of electrolyte decomposition. This decomposition voltage determines the upper electrochemical stability limit of the polymer electrolyte, which is crucial for its application in solid-state electrochemical devices. The relatively high stability up to 3.23 V suggests that CPL40 is suitable for moderate-voltage energy storage applications.[49]

The inset image shows the CPL40 electrolyte after the LSV study, displaying visible degradation. The structural deterioration confirms the breakdown of the polymer matrix upon exceeding the electrochemical stability threshold, highlighting the limitations of the electrolyte under prolonged high-voltage conditions.

3.2.6. Transference number study. The TNM studies were carried out to evaluate the total ionic and electronic contributions of the synthesized electrolyte. The ionic transference number t_{ion} was calculated using eqn (8), based on the DC polarization method. The corresponding current–time profile is shown in Fig. 11(b), where a sharp initial current drop followed by a steady-state plateau clearly demonstrates the ionic-dominated conduction behavior

$$t_{ion} = 1 - \frac{I_{final}}{I_{initial}} \quad (8)$$

where $I_{initial}$ and I_{final} denote the initial and steady-state currents obtained from the DC polarization curve, respectively.

The ionic conductivity σ_{ion} was then calculated using eqn (9):

$$\sigma_{ion} = \sigma_{bulk} \times t_{ion} \quad (9)$$

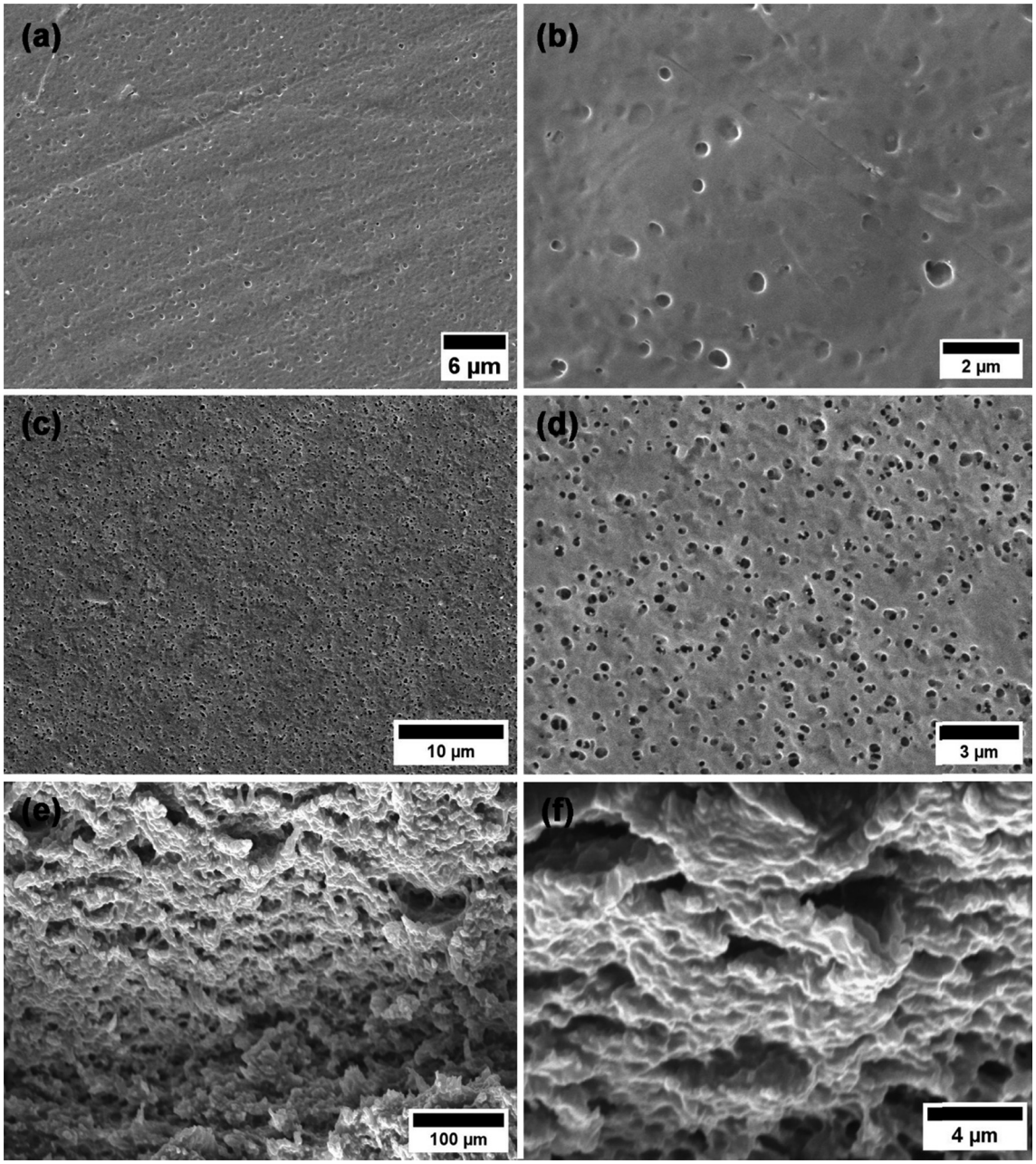

Fig. 9 SEM images of SPEs; (a) and (b) CP30 at different magnifications, (c) and (d) CPL40 at different magnifications, and (e) and (f) cross-sectional views of CPL40 at different magnifications.

where σ_{bulk} represents the bulk conductivity obtained from EIS and t_{ion} represents the measured transference number.

From the analysis, the calculated t_{ion} was 0.9856, indicating an ionic contribution of 98.56%. Accordingly, the ionic conductivity was determined to be 125 μS cm^{-1} and the electronic conductivity was 1.83 μS cm^{-1}, confirming the suitability of the electrolyte for solid-state electrochemical applications.

3.3. Performance analysis of EDLC devices

The performance was analyzed using standard electrochemical techniques including CV, GCD, cyclic stability and flexibility tests. These measurements provide insights into capacitive behavior, energy storage efficiency, long-term durability and flexibility of the device.

3.3.1. CV. The CV curves presented in Fig. S3(a) and (b) demonstrate the electrochemical behavior of the SC-1 and SC-2 devices under varying voltages ranging from 1.0 V to 1.5 V at a scan rate of 5 mV s^{-1} to determine the working potential of the EDLC device. The CV profiles show a gradual increase in current with increasing voltage, indicating enhanced electrochemical activity and charge transport within the system. The current response remains relatively small for voltages 1.0 V to 1.1 V, suggesting limited ion movement or electrode reaction kinetics. As the potential window increases beyond 1.2 V,

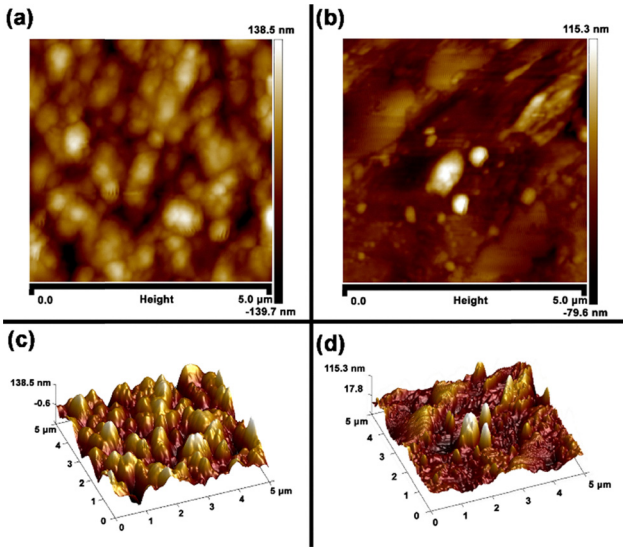

Fig. 10 AFM images of the samples: (a) CP30 and (b) CPL40 showing 2D height images, and (c) CPE30 and (d) CPL40 showing the corresponding 3D surface topography.

the current response increases progressively, signifying improved ionic conduction and charge transfer processes.

At 1.3 V, the CV curve exhibits a well-defined and stable profile, indicating an optimal balance between electrochemical activity and minimal polarization effects. Beyond 1.3 V, particularly at 1.4 V and 1.5 V, a sharper increase in current is observed, suggesting the start of side reactions or increased polarization, which could lead to reduced electrochemical stability over extended cycling. Based on this optimization analysis, in both cases (SC-1 and SC-2) 1.3 V is identified as the optimal operating voltage, ensuring stable charge–discharge cycling while maintaining efficient ion transport within the polymer electrolyte system.[50,51]

Although the CPL40 electrolyte showed a relatively wide electrochemical stability window of 3.23 V in the LSV measurement, the practical operating voltage of the assembled supercapacitor device was limited to 1.3 V. This difference occurs from the fundamental difference between LSV measurements and device-level electrochemical behavior. LSV is typically performed using inert blocking electrodes (SS|SPE|SS) and involves continuously increasing the potential until irreversible electrolyte decomposition occurs.[52] Therefore, the resulting voltage represents the intrinsic degradation limit of the electrolyte rather than the safe operating voltage of a practical device. In contrast, electrochemical measurements performed on the assembled supercapacitor reflect the behavior of the electrolyte within a practical electrode configuration (SS/AC|SPE|AC/SS (SC-1) and Cu/LIG|SPE|LIG/Cu (SC-2)). The porous electrode materials used in this study, such as AC and LIG, possess a significantly larger electrode–electrolyte interfacial area,[53] where polarization effects, ion transport limitations, and interactions with surface functional groups can promote parasitic reactions at lower potentials.[54] Consequently, although LSV provides the upper electrochemical stability limit of the electrolyte, device-level techniques such as cyclic voltammetry and long-term cycling are necessary to determine the practical operating voltage. In the present study, these measurements indicated increased current response and polarization effects at voltages exceeding 1.3 V, and therefore 1.3 V was selected as the optimal operating voltage to ensure stable electrochemical performance and long-term durability of the device.[55–57]

Fig. 12(a) shows the CV curves of SC-1 recorded at various scan rates ranging from 1 mV s^{-1} to 100 mV s^{-1}, demonstrating the electrochemical behaviour of the electrode material. The CV profiles maintain a quasi-rectangular shape at lower scan rates, indicating an ideal capacitive response with efficient charge storage through electric double-layer formation.[58] As the scan rate increases, the curves exhibit leaf like behaviour, likely due to increasing internal resistance and diffusion limitations within the electrode material. The nearly symmetrical CV loops across different scan rates confirm the stability and reversibility of the charge storage process.

In SC-2, based on the voltage-dependent CV analysis (Fig. S3(b)), 1.3 V was selected as the optimum practical operating voltage, as it provides the best compromise between

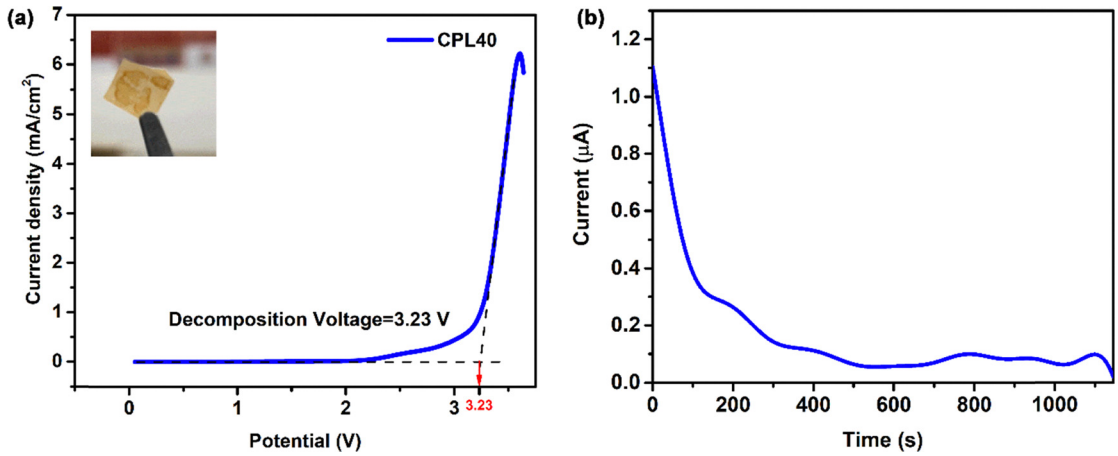

Fig. 11 (a) The LSV curve of CPL40 showing the electrochemical stability window with a decomposition voltage of 3.23 V. The inset image displays the degraded electrolyte. (b) DC polarization curve of the CS–PEG–$LiClO_4$ electrolyte under a 10 mV bias.

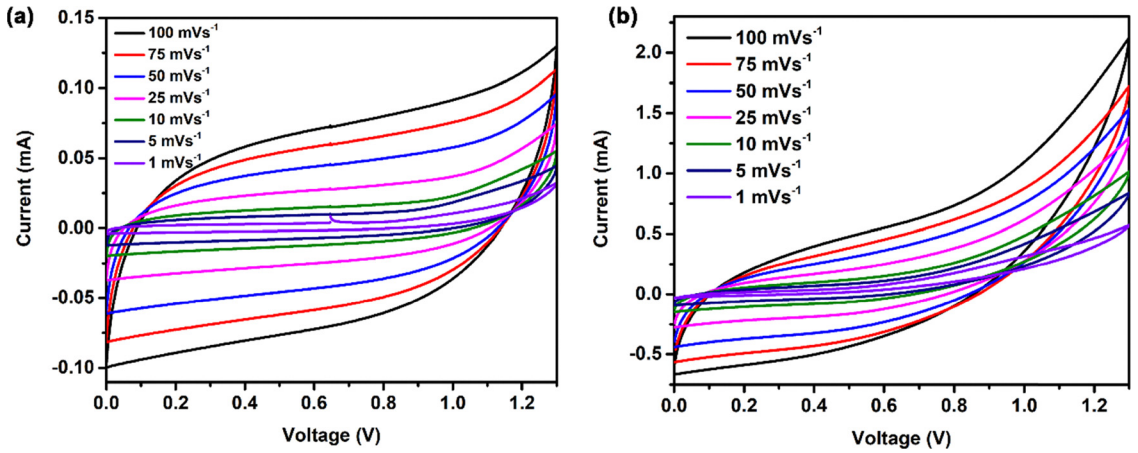

Fig. 12 CV curves: (a) SC-1 (activated carbon) and (b) SC-2 (LIG) at scan rates ranging from 1 mV s^{-1} to 100 mV s^{-1}.

higher current response and acceptable electrochemical distortion. Fig. 12(b) displays the CV curves of SC-2 recorded at different scan rates within this selected voltage window, showing quasi-capacitive behavior characteristic of EDLC charge storage. The relatively high current response of SC-2 arises from the highly porous and interconnected LIG structure, which provides a larger electrochemically accessible surface area and facilitates ion transport at the electrode–electrolyte interface.[59] However, the curves deviate from an ideal rectangular shape, particularly at higher potentials, where a pronounced tail indicates increasing polarization, internal resistance, and ion-transport limitations in the solid polymer electrolyte/LIG system. At lower scan rates, moderate widening and distortion of the loops are also observed, similar to SC-1, due to increased ohmic contribution and slower ionic mobility within the solid biopolymer electrolyte. Nevertheless, the CV response remains reproducible across all scan rates, indicating stable electrochemical operation within the selected voltage window.[60,61]

The specific capacitance (C_s) values and areal capacitance values (C_a), estimated from CV curves, are presented in Table 5 and show a decreasing trend with increasing scan rates. At a scan rate of 1 mV s^{-1}, the highest specific capacitance (C_s) of 5.98 F g^{-1} for SC-1 and an areal capacitance of 26.10 mF cm^{-2} for SC-2 were observed, indicating efficient charge accumulation due to extended ion diffusion time. However, as the scan rate increased to 100 mV s^{-1}, the capacitance values declined to 1.33 F g^{-1} for SC-1 and 3.69 mF cm^{-2} for SC-2. This decrease can be attributed to the limited time available for ion penetration into the deeper active sites of the electrode material at higher scan rates, which reduces charge storage efficiency.

Table 5 C_s of EDLCs estimated from CV at different scan rates

	Capacitance value	
Scan rate (mV s^{-1})	SC-1 (F g^{-1})	SC-2 (mF cm^{-2})
100	1.33	3.69
75	1.50	4.12
50	1.65	4.88
25	2.05	6.40
10	2.73	8.87
5	3.59	12.79
1	5.98	26.10

3.3.2. GCD. Fig. 13 presents the GCD profiles of SC-1 (Fig. 13a) and SC-2 (Fig. 13b) at varying current density ranging from 0.01 A g^{-1} to 0.1 A g^{-1} for SC-1 and 0.02 mA cm^{-2} to 0.25 mA cm^{-2} for SC-2. For SC-1, the nearly linear and symmetric charge–discharge curves demonstrate stable capacitive behavior with minimal resistive losses, confirming efficient charge storage within the CPL40 biopolymer electrolyte combined with activated carbon electrodes. As the current density increases, the discharge time shortens, indicating reduced charge storage capability due to restricted ion diffusion at higher charge–discharge time.[62]

Similarly, SC-2 exhibits well-defined, nearly triangular GCD curves with good symmetry across all current densities, highlighting the favorable capacitive response and low internal resistance of the LIG electrodes. The prolonged discharge times observed at lower current densities for SC-2 further support enhanced ion transport and efficient utilization of the electrode surface. Overall, these results confirm the reliable and stable electrochemical performance of both SC-1 and SC-2 devices under various current densities.

The discharge profiles exhibit longer retention times at lower current densities, indicating higher charge accumulation and improved capacitive performance. The capacitance values calculated from the GCD curves are summarized in Table 6. For SC-1 at 0.01 A g^{-1}, the highest specific capacitance of 5.32 F g^{-1} is observed, demonstrating enhanced charge storage efficiency at lower current densities, while SC-2 records a maximum areal capacitance of 18.83 mF cm^{-2} at 0.02 mA cm^{-2}. As the current density increases, the capacitance decreases to 0.12 F g^{-1} at 0.1 A g^{-1} for SC-1 and gradually declines for SC-2, likely due to diffusion constraints that limit accessibility to the active sites of the electrode. A noticeable IR drop is observed particularly at higher current densities, which can be attributed to internal resistance within the electrode–electrolyte system. This IR drop contributes to energy loss and indicates non-ideal behaviour under rapid charge–discharge conditions. The discharge time

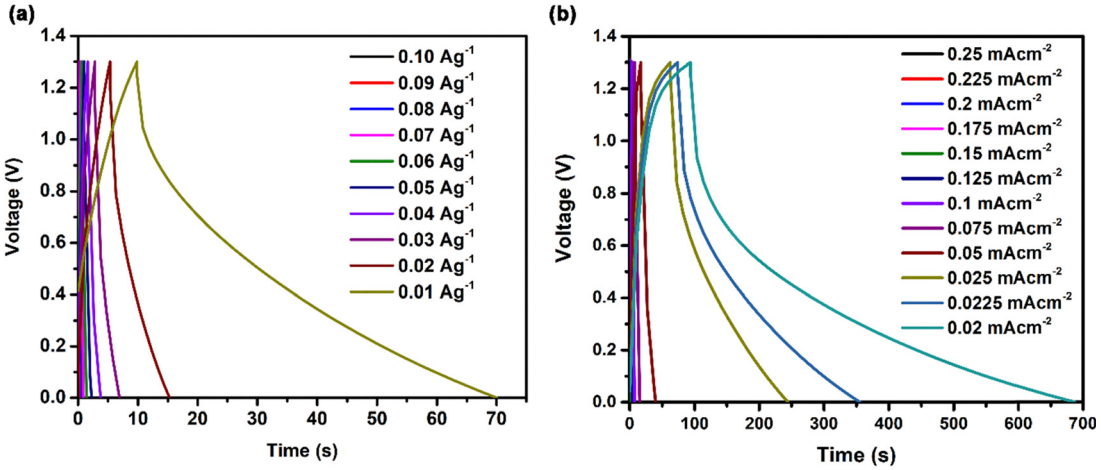

Fig. 13 GCD plots of (a) SC-1 at varying current density from 0.1 A g^{-1} to 0.01 A g^{-1} and (b) SC-2 at varying current density from 0.02 mA cm^{-2} to 0.25 mA cm^{-2}.

Table 6 C_s of EDLCs calculated from GCD at different current densities

SC-1		SC-2	
Current density (A g^{-1})	Specific capacitance (F g^{-1})	Current density (mA cm^{-2})	Areal capacitance (mF cm^{-2})
0.10	0.21	0.25	0.118
0.09	0.26	0.225	0.145
0.08	0.32	0.20	0.184
0.07	0.41	0.175	0.239
0.06	0.53	0.15	0.327
0.05	0.67	0.125	0.471
0.04	1.09	0.10	0.689
0.03	1.24	0.075	1.075
0.02	1.87	0.05	1.912
0.01	5.32	0.025	7.350
—	—	0.0225	10.17
—	—	0.02	18.83

becomes shorter at higher current densities, suggesting reduced 0charge storage capacity due to limited ion diffusion at faster charge–discharge rates.

3.3.3. EIS. The Nyquist plots of the devices are presented in Fig. 14. Fig. 14(a) corresponds to the AC based device (SC-1) and Fig. 14(b) represents the LIG-based device (SC-2) assembled with the CPL40 SPE.

For the AC based device (Fig. 14(a)), the impedance spectrum shows a small high-frequency intercept followed by a slanted capacitive line toward the low-frequency region, which is characteristic of porous carbon electrodes. The spectra were fitted using the equivalent circuit $R1 + Q2/(R2 + Q3)$. Here, the additional constant phase element ($Q3$) accounts for the distributed capacitive behavior arising from the highly porous activated carbon structure. In this model, $R1$ represents the series resistance (R_s) of the device, $Q1$ and $Q2$ correspond to the constant phase elements describing the non-ideal capacitive behavior of the porous electrode and electrode–electrolyte interface, and $R2$ denotes the interfacial resistance. The fitting yielded R_s = 81.53 Ω and $R2$ = 411.2 Ω, with a normalized χ^2 value of 4.60×10^{-3}, indicating a good agreement between the experimental and fitted data.

For the LIG-based device (Fig. 14(b)), a similar intercept followed by a capacitive tail is observed, reflecting the porous and conductive nature of the LIG electrode. The impedance data were fitted using the equivalent circuit $R1 + Q2/(R2 + W)$,

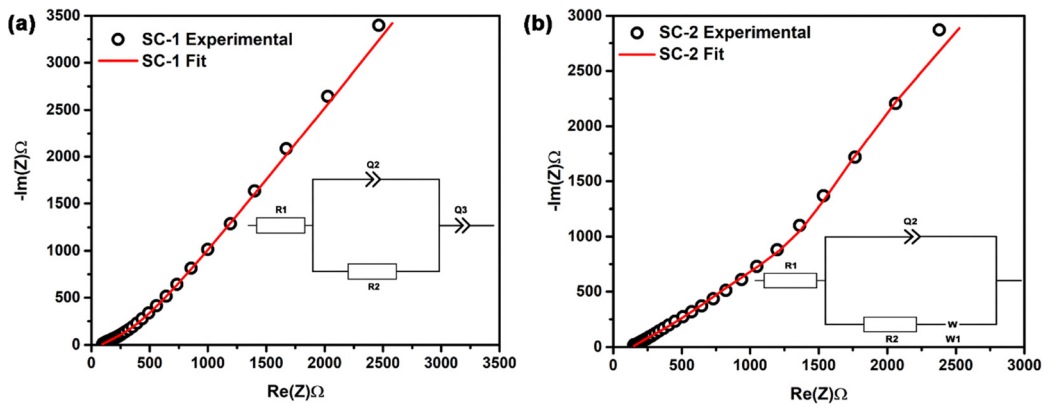

Fig. 14 Nyquist plots of the (a) SC-1 and (b) SC-2 based device with the CPL40 SPE with the equivalent circuits.

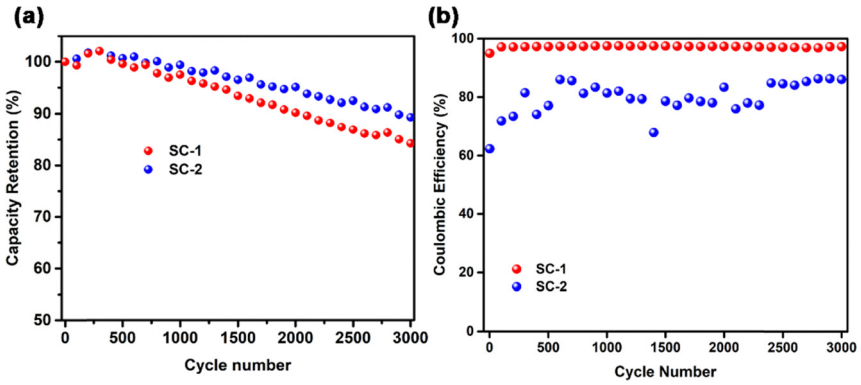

Fig. 15 Long-term cycling performance of the supercapacitor devices: (a) capacitance retention and (b) coulombic efficiency of SC-1 and SC-2 over 3000 charge–discharge cycles.

where the Warburg element (W) represents ion diffusion within the interconnected porous graphene network. The obtained parameters include R_s = 36.08 Ω and $R2$ = 182.4 Ω, with a normalized χ^2 value of 0.1145, indicating an acceptable fit for the porous electrode system.

Overall, the EIS results confirm that both devices exhibit capacitive-dominated electrochemical behavior, while the LIG electrode shows lower series and interfacial resistances, suggesting improved ion transport and charge transfer characteristics compared to the activated carbon electrode.

3.3.4. Cyclic stability studies of the devices. Fig. 15 shows the variation in Coulombic efficiency (%) as a function of the cycle number for the two supercapacitors SC-1 and SC-2. SC-1 exhibits near-ideal coulombic efficiency, consistently maintaining values close to 97% throughout the entire cycling, indicating highly reversible charge storage processes and minimal parasitic side reactions. However, SC-2 shows comparatively lower and more fluctuating efficiency values, stabilizing in the 85% range after 3000 cycles. The slightly lower and more fluctuating coulombic efficiency observed for SC-2 can be due to the highly porous and defect-rich structure of LIG where non-uniform pore distribution and the binder-free electrode architecture may introduce localized polarization effects and minor irreversible charge losses during repeated cycling.

The electrochemical performance of SC-1 and SC-2 can be comprehensively understood in terms of their underlying structural and electronic characteristics, as reflected in the CV, GCD, and EIS analyses.

Structurally, the AC electrode used in SC-1 exhibits a microporous, powder-based morphology with a high specific surface area, which facilitates efficient electric double-layer formation and stable ion movement. The presence of a PVDF binder improves mechanical integrity and maintains consistent electrode–electrolyte contact during repeated cycling, resulting in stable electrochemical behavior and a coulombic efficiency of about 97%. In contrast, the LIG electrode in SC-2 is a binder-free, three-dimensional interconnected graphene network with accessible porous channels for ion transport. However, its defect-rich nature and non-uniform pore distribution can introduce localized polarization and interfacial instability, leading to a comparatively lower and more fluctuating coulombic efficiency of about 85%.

From an electronic perspective, EIS provides quantitative insight into charge transport and interfacial kinetics. The Nyquist plots (Fig. 14) show that SC-2 has much lower resistance values, with R_s = 36.08 Ω and R_{ct} = 182.4 Ω, compared to SC-1 (R_s = 81.53 Ω and R_{ct} = 411.2 Ω). This improved conductivity is attributed to the continuous graphene network in LIG, which supports efficient electron transport and faster charge-transfer kinetics, whereas the higher resistance in SC-1 arises from interparticle contact limitations in the powder-based AC electrode.

These differences are reflected in electrochemical behavior. SC-1 shows a more ideal CV shape and symmetric GCD response, indicating stable capacitive performance, whereas SC-2 exhibits distortion at higher potentials and lower coulombic efficiency due to polarization and interfacial losses. Overall, activated carbon offers structural robustness and stable capacitive behavior, while LIG provides faster charge transport and higher conductivity, but with greater susceptibility to polarization.

3.3.5. Mechanical flexibility studies for the fabricated device. The mechanical durability of the fabricated flexible solid-state supercapacitor under repeated bending conditions is presented in Fig. 16. In Fig. 16(a), CV curves recorded at 10 mV s^{-1} across 500 bending cycles display quasi-rectangular and nearly symmetric profiles, indicating a preserved electric double-layer capacitive mechanism and stable ionic transport behaviour. The absence of significant distortion or redox features after repeated bending suggests that the electrode–electrolyte interface retains its structural and functional integrity under mechanical stress.

The capacitance retention shown in Fig. 16(b) tells that the device maintains 97.5% of its initial capacitance after 500 bending cycles, reflecting exceptional electrochemical stability and mechanical endurance, both of which are critical for reliable flexible and wearable energy storage systems.

Fig. 16(c) illustrates GCD curves at a current density of 0.2 mA cm^{-2} before and after 500 bending cycles. The device achieves a capacitance retention of 97.8%, highlighting the robust

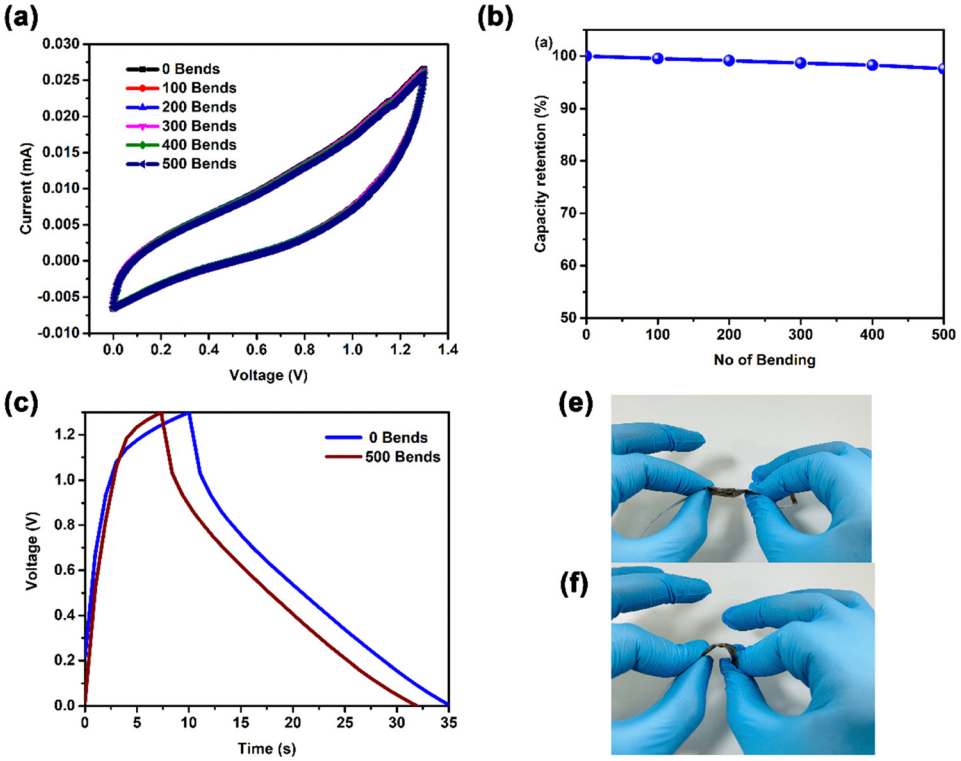

Fig. 16 (a) CV curves of the flexible supercapacitor device recorded at 10 mV s^{-1} across 0 to 500 bending cycles. (b) Capacity retention as a function of bending cycles. (c) GCD curves at a current density of 0.05 mA cm^{-2} before and after 500 bending cycles. (e) Photographs of the fabricated flexible device: (e) before bending (178°) and (f) during bending (75°).

charge–discharge kinetics and sustained ionic conduction pathways despite repeated flexural deformation. Additionally, Fig. 16(e) and (f) provide direct photographic evidence of the device before and after a single bending cycle, with no observable mechanical delamination or fracture. This outcome substantiates the better mechanical flexibility and structural stability of the supercapacitor architecture. Collectively, these results confirm that the proposed flexible solid-state supercapacitor demonstrates outstanding mechanical durability and stable electrochemical performance.

Overall, these results highlight the good long-term cycling durability and high Coulombic efficiencies of both devices, supporting their suitability for flexible solid-state supercapacitor applications. The detailed electrochemical performance parameters of SC-1 and SC-2 are given in Table 7 and Table 8, respectively.

The capacitance values of SC-1 and SC-2 are reported using different normalization methods because the two devices represent distinct electrode configurations. For SC-1, which is based on powdered activated carbon electrodes, the capacitance is expressed as gravimetric specific capacitance (F g^{-1}). In contrast, SC-2 is a flexible, binder-free planar supercapacitor based on LIG formed directly on a PI substrate. Since LIG is generated *in situ* and remains strongly adhered to the PI substrate, it cannot be practically separated and weighed independently without damaging the electrode structure. Therefore, areal capacitance (F cm^{-2}) is the more appropriate metric for evaluating SC-2 and is commonly used for planar and flexible LIG-based devices.

Table 7 Comparison of electrochemical performance parameters of SC-1

Parameters	SC-1
Specific capacitance at a scan rate of 1 mV s^{-1} obtained from CV (F g^{-1})	5.50
Specific capacitance at a current density of 0.01 mA g^{-1} obtained using GCD (F g^{-1})	5.32
Energy density (Wh kg^{-1})	1.13
Power density (W kg^{-1})	68.49
Capacity retention (%) at the end of 3000 cycles	84.20
Coulombic efficiency (%) at the end of 3000 cycles	97.27

Table 8 Comparison of electrochemical performance parameters of SC-2

Parameters	SC-2
Areal capacitance at a scan rate of 1 mV s^{-1} obtained from CV (mF cm^{-2})	26.100
Areal capacitance at a current density of 0.02 mA cm^{-2} obtained using GCD (mF cm^{-2})	18.830
Energy density (μWh cm^{-2})	4.150
Power density (mW cm^{-2})	0.025
Capacity retention (%) at the end of 3000 cycles	89.300
Coulombic efficiency (%) at the end of 3000 cycles	86.063
Bending test (%) at the end of 500 bending cycles	97.500

3.4. Ion transport mechanism

In Fig. 17, SC-1 represents the activated carbon-based nonflexible device and SC-2 represents the flexible device fabricated using LIG. Both the devices consist of a hybrid polymer electrolyte made from CS and PEG doped with $LiClO_4$. The flexible chains of PEG host oxygen atoms that temporarily bind to Li^+ ions, helping them break free from ClO_4^- anions and move through the electrolyte. Chitosan adds another layer of functionality, in that its hydroxyl and amine groups also coordinate Li^+, while its natural backbone strengthens the electrolyte and forms hydrogen bonds with ClO_4^-, keeping ion movement stable over time.

In SC-1, a stainless-steel sheet is coated with a mixture of activated carbon and binder. The large surface area of activated carbon provides easy access for ions. On the other hand, the CS–PEG network ensures Li^+ can travel efficiently between electrodes. Here, ion motion mainly follows the PEG-coordination pathways, with CS ensuring structural reinforcement and reducing anion–cation recombination. In SC-2, the electrode is built differently. A polyimide sheet is patterned into LIG using a CO_2 laser. The LIG features a sponge-like network of interconnected pores that the SPEs penetrate, enabling conformal interfacial contact and efficient transport pathways. Even when the device is bent, the LIG structure bends without losing contact with the electrolyte, keeping transport pathways open. The rigidity caused due to bending in the SPEs is compensated with the flexibility of LIG. SC-2, in particular, benefits from the LIG's ability to let ions flow in multiple directions, making it a strong candidate for flexible, wearable, and long-lasting energy storage devices.

3.5. Comparative analysis with existing studies

Recent studies have explored alternative polymer blends and doping strategies to enhance the ionic conductivity of CS-based electrolytes further. For instance, Samsudin *et al.* investigated an alginate–PVA-based polymer electrolyte with Li^+ charge carriers for supercapacitor applications, achieving improved electrochemical performance.[63] Similarly, Fadzallah *et al.* studied CS–oxalic acid solid polymer electrolytes and identified the relaxation process that influences their conductivity.[64] Nayak *et al.* developed an eco-friendly CS–dextran polyblend electrolyte for primary magnesium batteries, demonstrating enhanced ionic conductivity and improved performance.[65] Additionally, Rathod *et al.* conducted extensive studies on lithium perchlorate-doped PVA/CS composites, reporting improved conductivity due to optimized transport parameters.[66] In a related study, Rathod *et al.* further examined $LiClO_4$-doped PVA/CS composites, highlighting their ionic

Table 9 Comparison of the ionic conductivity, electrochemical stability, and capacitance of reported biopolymer-based SPEs with this work

SPE system	IC (μS cm^{-1})	LSV (V)	C_s (F g^{-1})	Ref.
CS-oxalic acid	0.49	—	—	64
CS–dextran–$Mg(ClO_4)_2$	699.00	2.66	—	65
CS–PVA–$LiClO_4$	300.00	—	—	66
CS–PVA–$LiClO_4$	86.10	—	—	67
CS–PEG (35000)–$LiClO_4$	110.00			11
CS–PEG–$LiClO_4$	127.00	3.23	5.1	This work

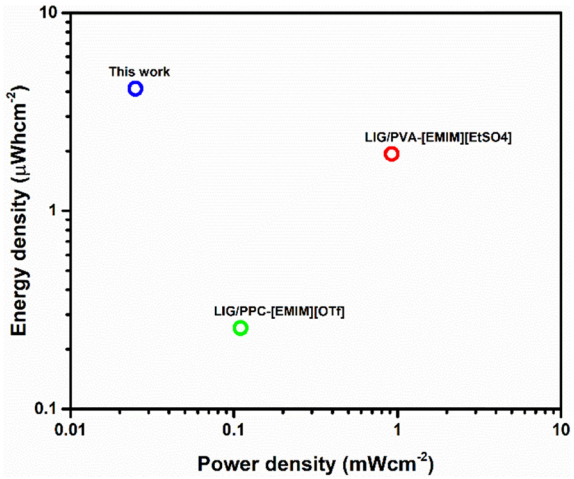

Fig. 18 Ragone plot comparing the areal energy density and power density of the LIG-based supercapacitor developed in this work with previously reported LIG-based supercapacitors LIG/PVA–[EMIM][$EtSO_4$][68] and LIG/PPC–[EMIM][OTf].[68]

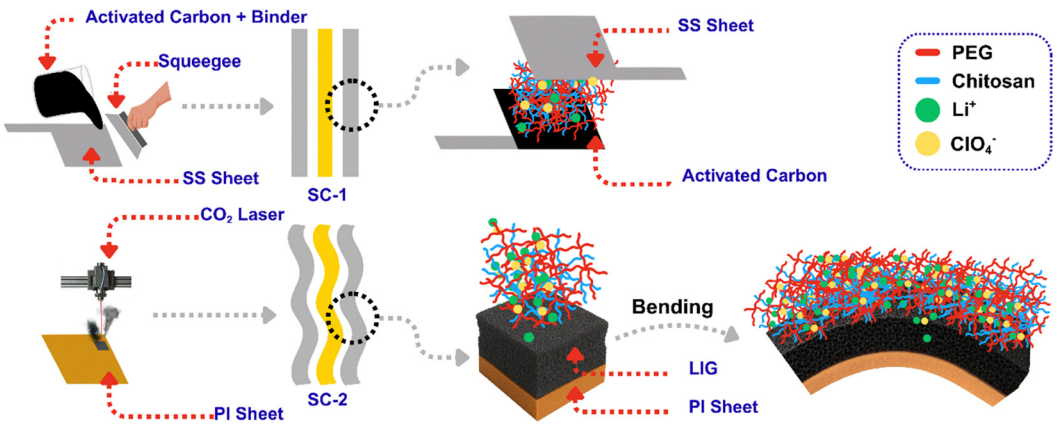

Fig. 17 Illustration of the CPL electrolyte mechanism in activated carbon (SC-1) and LIG (SC-2) supercapacitors.

Table 10 Areal capacitance (C_a), energy density (E_D), power density (P_D), and cyclic stability (CS) of LIG-based supercapacitors with various polymer electrolytes

Electrode	Electrolyte	C_a (mF cm^{-2})	E_D (μWh cm^{-2})	P_D (mW cm^{-2})	CS (%)	Ref.
LIG	PVA/[EMIM][EtSO$_4$]	15.10 @ 2 mA cm^{-2}	1.94	0.92	80	68
LIG	PVA/H$_2$SO$_4$	13.27 @ 0.05 mA cm^{-2}	—	—	103	69
LIG	PVA/H$_2$SO$_4$	9 @ 0.02 mA cm^{-2}	—	—	98	70
LIG	PPC/[EMIM][OTf]	1.75 @ 5.0 mV s^{-1}	0.256	0.11	98	71
LIG	CS–PEG–LiClO$_4$	18.83 @ 0.02 mA cm^{-2}	4.150	0.025	86	This work

conductivity and dielectric properties, which are essential for their practical application in energy storage devices.[67] The outcome of all these studies is summarized in Table 9. The CS–PEG–LiClO$_4$ system developed in this work shows a well-balanced performance compared to other reported biopolymer-based SPEs. While some systems offer higher ionic conductivity, they lack data on electrochemical stability or capacitance. In contrast, our system delivers moderate conductivity (127 μS cm^{-1}), a broader electrochemical window (3.23 V), and a specific capacitance of 5.1 F g^{-1}. This combination of properties highlights its potential for safe and efficient use in energy storage applications.

A comparison with previously reported LIG-based supercapacitors using different polymer electrolytes is presented. To further evaluate the electrochemical performance of the assembled supercapacitor device, a Ragone plot was constructed using the calculated energy density and power density values. As shown in Fig. 18, the LIG-based supercapacitor developed in this work delivers an areal energy density of approximately 4.15 μWh cm^{-2} at a power density of 0.025 mW cm^{-2}, which is higher than previously reported LIG-based supercapacitors employing polymer electrolytes such as PVA–[EMIM][EtSO$_4$] and PPC–[EMIM][OTf]. Although the power density of the present device is relatively low, the significantly improved energy density indicates enhanced charge storage capability, which can be attributed to the efficient ion transport and strong interfacial interaction provided by the CS–PEG–LiClO$_4$ polymer electrolyte. These results demonstrate the potential of the developed electrolyte system for high-energy flexible supercapacitor applications (Table 10). The LIG/PVA/[EMIM][EtSO$_4$] system exhibits an areal capacitance of 15.10 mF cm^{-2} with an energy density of 1.94 μWh cm^{-2}, while LIG/PVA/H$_2$SO$_4$ shows 13.27 mF cm^{-2} but without reported energy and power densities. In contrast, LIG/PPC/[EMIM][OTf] delivers a much lower capacitance of 1.75 mF cm^{-2} despite excellent cycling stability.

Notably, the LIG device using the CS–PEG–LiClO$_4$ electrolyte in this work achieves a higher areal capacitance of 18.83 mF cm^{-2} and a significantly improved energy density of 4.150 μWh cm^{-2}. This enhanced performance can be attributed to the synergistic polymer network of chitosan and PEG, which facilitates better ion transport, along with the high mobility of Li$^+$ ions from LiClO$_4$, leading to improved charge storage at the LIG electrode interface.

4. Conclusion

In this study, a sustainable and biodegradable SPE system based on CS and PEG, doped with LiClO$_4$, was systematically developed, characterized, and evaluated for flexible electrochemical energy storage applications. The optimized CS–PEG blend, followed by Li$^+$ incorporation, resulted in a composition (CPL40) with enhanced ionic conductivity (127 μS cm^{-1}) and a wide electrochemical stability window up to 3.23 V. FTIR and XRD analysis confirmed strong polymer–salt interactions and an increased amorphous nature conducive to ion transport. Thermal analysis showed improved segmental mobility, while morphological studies indicated a well-connected porous architecture supporting ion diffusion.

The fabricated supercapacitor devices (SC-1 and SC-2) exhibited promising specific capacitances of 5.32 F g^{-1} and 18.83 mF cm^{-2} at low current densities, along with excellent cyclic stability, retaining up to 84.2% and 89.3% capacitance over 3000 charge–discharge cycles. Furthermore, the devices maintained superior electrochemical behaviour under repeated mechanical bending, achieving 97.5% capacitance retention after 500 bending cycles and conserving their structural integrity. These findings confirm that the CS–PEG–LiClO$_4$ SPEs are a promising eco-compatible and scalable platform for next-generation flexible and safe solid-state supercapacitors. Future studies may focus on further optimizing the polymer–salt interactions and integrating functional nanofillers to push the boundaries of ionic conductivity and mechanical durability.

Conflicts of interest

The authors declare that they have no known competing financial interests or personal relationships that could have influenced the work reported in this paper.

Data availability

The data supporting this article have been included as part of the supplementary information (SI). The supplementary information includes additional experimental details. See DOI: https://doi.org/10.1039/d6ma00162a.

Acknowledgements

The authors thank the Device Fabrication and Characterization Lab (DFCL), School of Electrical Engineering, Manipal Institute of Technology, Manipal Academy of Higher Education, for providing the necessary laboratory facilities and instrumentation support throughout this study. The authors thank Ms Ankitha Rao and Dr Shounak De for their sincere assistance

and cooperation during material preparation and electrochemical analysis. The authors acknowledge the use of ChatGPT (OpenAI) for assistance in grammar checking and correction of typographical errors during manuscript preparation.

References

1 S. Raza, A. Hayat, T. Bashir, C. Chen, L. Shen, Y. Orooji and H. Lin, *Sustainable Mater. Technol.*, 2024, **40**, e00963.
2 R. Sharma, H. Kumar, G. Kumar, S. Sharma, R. Aneja, A. K. Sharma, R. Kumar and P. Kumar, *Chem. Eng. J.*, 2023, **468**, 143706.
3 J. B. Goodenough, *Energy Environ. Sci.*, 2014, **7**, 14–18.
4 G. G. Farivar, W. Manalastas, H. D. Tafti, S. Ceballos, A. Sanchez-Ruiz, E. C. Lovell, G. Konstantinou, C. D. Townsend, M. Srinivasan and J. Pou, *Proc. IEEE*, 2023, **111**, 397–420.
5 A. A. Kebede, T. Kalogiannis, J. Van Mierlo and M. Berecibar, *Renewable Sustainable Energy Rev.*, 2022, **159**, 112213.
6 J. R. Miller, R. A. Outlaw and B. C. Holloway, *Electrochim. Acta*, 2011, **56**, 10443–10449.
7 P. Sharma and T. S. Bhatti, *Energy Convers. Manage.*, 2010, **51**, 2901–2912.
8 T. Ye, L. Li and Y. Zhang, *Adv. Funct. Mater.*, 2020, **30**(29), 2000077(1)–2000077(20).
9 X. Fan, C. Zhong, J. Liu, J. Ding, Y. Deng, X. Han, L. Zhang, W. Hu, D. P. Wilkinson and J. Zhang, *Chem. Rev.*, 2022, **122**, 17155–17239.
10 P. Mahajan and M. Sharma, *Energy Storage*, 2024, **6**(4), 1–24.
11 Y. N. Sudhakar and M. Selvakumar, *J. Appl. Electrochem.*, 2013, **43**, 21–29.
12 V. Cyriac, Ismayil, I. S. B. M. Noor, Z. E. Rojudi, Y. N. Sudhakar, C. Chavan, R. F. Bhajantri and M. S. Murari, *Int. J. Energy Res.*, 2022, **46**, 22845–22866.
13 S. Kaur and G. S. Dhillon, *Crit. Rev. Microbiol.*, 2014, **40**, 155–175.
14 J. B. Marroquin, K. Y. Rhee and S. J. Park, *Carbohydr. Polym.*, 2013, **92**, 1783–1791.
15 R. Kumar and S. A. Suthanthiraraj, *J. Solid State Electrochem.*, 2014, **18**, 1647–1656.
16 T. R. Kartha and B. S. Mallik, *J. Mol. Liq.*, 2020, **302**, 112536.
17 W. Ma, S. Chen, S. Yang, W. Chen, W. Weng and M. Zhu, *ACS Appl. Mater. Interfaces*, 2016, **8**, 14622–14627.
18 J. Lin, Z. Peng, Y. Liu, F. Ruiz-Zepeda, R. Ye, E. L. G. Samuel, M. J. Yacaman, B. I. Yakobson and J. M. Tour, *Nat. Commun.*, 2014, **5**, 5714.
19 R. Ye, D. K. James and J. M. Tour, *Acc. Chem. Res.*, 2018, **51**, 1609–1620.
20 F. Clerici, M. Fontana, S. Bianco, M. Serrapede, F. Perrucci, S. Ferrero, E. Tresso and A. Lamberti, *ACS Appl. Mater. Interfaces*, 2016, **8**, 10459–10465.
21 Z. Peng, J. Lin, R. Ye, E. L. G. Samuel and J. M. Tour, *ACS Appl. Mater. Interfaces*, 2015, **7**, 3414–3419.
22 L. Li, J. Zhang, Z. Peng, Y. Li, C. Gao, Y. Ji, R. Ye, N. D. Kim, Q. Zhong, Y. Yang, H. Fei, G. Ruan and J. M. Tour, *Adv. Mater.*, 2016, **28**, 838–845.
23 J. Zhao, S. Wang, L. Gao, D. Zhang, Y. Guo and R. Xu, *ACS Appl. Nano Mater.*, 2022, **5**, 11314–11323.
24 C. Zhu, X. Dong, X. Mei, M. Gao, K. Wang and D. Zhao, *J. Mater. Sci.*, 2020, **55**, 17108–17119.
25 J. R. J. UC, S. Bhat, Y. N. Sudhakar, A. Rao, V. Cyriac and S. De, *J. Mater. Sci.*, 2025, **60**, 10944–10964.
26 J. Wang, S. Song, S. Gao, R. Muchakayala, R. Liu and Q. Ma, *Polym. Test.*, 2017, **62**, 278–286.
27 P. Nayak, Ismayil, V. Cyriac, S. Hegde, G. Sanjeev, M. S. Murari and Y. N. Sudhakar, *J. Non.-Cryst. Solids*, 2022, **592**, 121741.
28 L. Ojeda, J. Oliva, A. Encinas, A. I. Mtz-Enriquez, P. C. H. del Castillo, J. P. Quintero and E. Muñoz-Sandoval, *J. Appl. Electrochem.*, 2025, **55**, 3115–3130.
29 Y. Gao, *Nanoscale Res. Lett.*, 2017, **12**, 387.
30 V. Cyriac, Ismayil, K. Mishra, A. Rao, R. A. Khellouf, S. P. Masti and I. M. Noor, *Mater. Adv.*, 2025, **6**, 3149–3170.
31 A. Rao, S. Bhat, S. De and V. Cyriac, *J. Energy Storage*, 2024, **102**, 113965.
32 M. Sharma and S. Yashonath, *J. Chem. Phys.*, 2008, **129**(14), 144103.
33 L. Sampathkumar, P. Christopher Selvin, S. Selvasekarapandian, P. Perumal, R. Chitra and M. Muthukrishnan, *Ionics*, 2019, **25**, 1067–1082.
34 Y. Li, J. Wang, J. Tang, Y. Liu and Y. He, *J. Power Sources*, 2009, **187**, 305–311.
35 R. He and T. Kyu, *Macromolecules*, 2016, **49**, 5637–5648.
36 H. S. Koker, H. Yavuz Ersan and A. Aytac, *Iran. Polym. J.*, 2023, **32**, 263–273.
37 P.-Y. Pennarun and P. Jannasch, *Solid State Ionics*, 2005, **176**, 1103–1112.
38 T. Alonso-García, M. J. Rodríguez-Presa, C. Gervasi, S. Moya and O. Azzaroni, *Anal. Chem.*, 2013, **85**, 6561–6565.
39 Y. M. Yusof, H. A. Illias and M. F. Z. Kadir, *Ionics*, 2014, **20**, 1235–1245.
40 A. Aradmehr and V. Javanbakht, *Colloids Surf., A*, 2020, **600**, 124952.
41 Z. A. Raza, A. Mobeen, M. S. ur Rehman and M. I. Majeed, *Polym. Bull.*, 2023, **80**, 11031–11047.
42 R. N. Sagar, R. Vasachar and S. Hegde, *eXPRESS Polym. Lett.*, 2023, **17**, 883–899.
43 D. Bharati and A. Saroj, *Polym.-Plast. Technol. Mater.*, 2023, **62**, 989–1007.
44 I. A. Fadzallah, S. R. Majid, M. A. Careem and A. K. Arof, *Ionics*, 2014, **20**, 969–975.
45 S. B. Aziz, T. J. Woo, M. F. Z. Kadir and H. M. Ahmed, *J. Sci.: Adv. Mater. Devices*, 2018, **3**, 1–17.
46 A. Arya and A. L. Sharma, *J. Solid State Electrochem.*, 2018, **22**, 2725–2745.
47 K. M. Manikandan, A. Yelilarasi, P. Senthamaraikannan, S. S. Saravanakumar, A. Khan and A. M. Asiri, *J. Solid State Electrochem.*, 2018, **22**, 3785–3797.
48 V. Cyriac, Ismayil, K. Mishra, A. Rao, S. P. Masti and I. M. Noor, *Energy Technol.*, 2025, **13**(11), 2500465.
49 S. B. Aziz, E. M. A. Dannoun, M. H. Hamsan, H. O. Ghareeb, M. M. Nofal, W. O. Karim, A. S. F. M. Asnawi, J. M. Hadi and M. F. Z. A. Kadir, *Polymers*, 2021, **13**, 930.

50 N. L. Torad, R. R. Salunkhe, Y. Li, H. Hamoudi, M. Imura, Y. Sakka, C. Hu and Y. Yamauchi, *Chem. – Eur. J.*, 2014, **20**, 7895–7900.
51 J. Yu, N. Fu, J. Zhao, R. Liu, F. Li, Y. Du and Z. Yang, *ACS Omega*, 2019, **4**, 15904–15911.
52 K. Xu, S. P. Ding and T. R. Jow, *J. Electrochem. Soc.*, 1999, **146**, 4172–4178.
53 P. Ruschhaupt, S. Pohlmann, A. Varzi and S. Passerini, *Batteries Supercaps*, 2020, **3**, 698–707.
54 K. Xu, S. P. Ding and T. R. Jow, *J. Electrochem. Soc.*, 1999, **146**, 4172–4178.
55 P. Pal, S. K. Patla and A. Ghosh, *ACS Appl. Energy Mater.*, 2025, **8**, 8950–8962.
56 N. Ahmad, A. Rinaldi, M. Setti, M. Sidoli, S. Scaravonati, V. Vezzoni, G. Magnani, M. Riccò, C. Milanese, M.-M. Titirici and D. Pontiroli, *ACS Appl. Energy Mater.*, 2025, **8**, 9391–9406.
57 V. Cyriac, Ismayil, K. Mishra, A. Rao, R. A. Khellouf, S. P. Masti and I. M. Noor, *Mater. Adv.*, 2025, **6**, 3149–3170.
58 I. Ruti, V. Kaliyaperumal, R. Kola, D. Pratap Rao and S. Kumar, *Mater. Lett.*, 2024, **376**, 137131.
59 R. Ye, D. K. James and J. M. Tour, *Adv. Mater.*, 2019, **31**, 1803621.
60 P. K. Katkar, S. J. Marje, V. G. Parale, C. D. Lokhande, J. L. Gunjakar, H.-H. Park and U. M. Patil, *Langmuir*, 2021, **37**, 5260–5274.
61 P. Sharma, D. Singh, M. Minakshi, S. Quadsia and R. Ahuja, *ChemPlusChem*, 2022, **87**(6), 1–14.
62 R. Tian, S.-H. Park, P. J. King, G. Cunningham, J. Coelho, V. Nicolosi and J. N. Coleman, *Nat. Commun.*, 2019, **10**, 1933.
63 A. S. Samsudin, N. M. Ghazali, N. F. Mazuki, K. Aoki and Y. Nagao, *J. Electroanal. Chem.*, 2024, **967**, 118463.
64 I. A. Fadzallah, S. R. Majid, M. A. Careem and A. K. Arof, *Ionics*, 2014, **20**, 969–975.
65 P. Nayak and Ismayil, *Energy Technol.*, 2024, **12**(10), 2400866.
66 S. G. Rathod, R. Bhajantri, V. Ravindrachary, B. Poojary, P. Pujari, T. Sheela and J. Naik, *J. Elastomers Plast.*, 2016, **48**, 442–455.
67 S. G. Rathod, R. F. Bhajantri, V. Ravindrachary, P. K. Pujari and T. Sheela, *J. Adv. Dielectr.*, 2014, **04**, 1450033.
68 A. Rao, S. Bhat, S. De, V. Cyriac and A. Rag S, *J. Energy Storage*, 2023, **68**, 107716.
69 T. Lu, A. Adiraju, Y. Li, H. Mo, Z. Wu and O. Kanoun, *International Workshop on Impedance Spectroscopy (IWIS)*, 2024, pp. 85–89.
70 Z. Peng, J. Lin, R. Ye, E. L. G. Samuel and J. M. Tour, *ACS Appl. Mater. Interfaces*, 2015, **7**, 3414–3419.
71 A. Ray, J. Roth and B. Saruhan, *Molecules*, 2022, **27**, 329.